JGR Oceans

RESEARCH ARTICLE
10.1029/2020JC016174

Structure and Transport of Atlantic Water North of Svalbard From Observations in Summer and Fall 2018

Eivind H. Kolås[1], Zoé Koenig[1,2], Ilker Fer[1], Frank Nilsen[3,1], and Marika Marnela[3]

[1]Geophysical Institute, University of Bergen and Bjerknes Center for Climate Research, Bergen, Norway, [2]Norwegian Polar Institute, Tromsø, Norway, [3]The University Center in Svalbard, Longyearbyen, Norway

Key Points:
- The average Atlantic Water inflow in summer and fall 2018 was 2.6 Sv, reaching 3 Sv in October
- A recirculation in the Sofia Deep transports (0.1–0.2 Sv) Atlantic Water westward
- A deep, bottom-intensified current on the lower continental slope carries cold waters into the Arctic

Correspondence to:
E. H. Kolås,
eivind.kolas@uib.no

Citation:
Kolås, E. H., Koenig, Z., Fer, I., Nilsen, F., & Marnela, M. (2020). Structure and transport of Atlantic Water north of Svalbard from observations in summer and fall 2018. *Journal of Geophysical Research: Oceans*, *125*, e2020JC016174. https://doi.org/10.1029/2020JC016174

Received 21 FEB 2020
Accepted 16 AUG 2020
Accepted article online 20 AUG 2020

Abstract The transport of warm Atlantic Waters north of Svalbard is one of the major heat and salt sources to the Arctic Ocean. The circulation pathways and the associated heat transport influence the variability in the Arctic sea ice extent, the onset of freezing, and marine ecosystems. We present observations obtained from research cruises and an autonomous underwater glider mission in summer and fall 2018, to describe the hydrographic structure, volume transport, and circulation patterns of the warm Atlantic Water Boundary Current between 12°E and 24°E north of Svalbard. The Atlantic Water volume transport reaches a maximum of 3.0 $\pm$0.2 Sv in October, with an intraseasonal variability of 1 Sv (1 Sv = 10^6 m^3 s^{-1}). During summer and late fall, we observed an Atlantic Water recirculation flowing westward (0.1–0.2 Sv) in the outer part of the section away from the shelf break. This counter current appears to be a part of an anticyclonic circulation in the Sofia Deep. The strength of the Atlantic Water recirculation and the Atlantic Water boundary current is very sensitive to the wind stress curl: The boundary current volume transport doubled in less than a week, corresponding to a transition from strongly negative (-10^{-6} N m^{-3}) to strongly positive (10^{-6} N m^{-3}) wind stress curl over the Sofia Deep. A previously unknown, deep bottom-intensified current is observed to flow parallel to the boundary current, between the 1,500 and 2,000 m isobaths. Historical data in the region support the presence of the bottom-intensified current.

Plain Language Summary Atlantic Water enters the Arctic Ocean along two pathways, through the Barents Sea and through Fram Strait west of Svalbard. Being warmer and saltier than the Arctic Ocean, the Atlantic Water is the main heat and salt source for the Arctic Ocean. The circulation pathways and the heat transported by the Atlantic Water influence the variability of the Arctic sea ice and the marine ecosystems. We present observations from research cruises and an autonomous underwater glider mission in summer and fall 2018, to describe the Atlantic Water structure and circulation between 12°E and 24°E north of Svalbard (an extension of the Fram Strait inflow). The Atlantic Water volume transport reaches a maximum of 3.0 $\pm$0.2 Sv in October, with an intraseasonal variability of 1 Sv (1 Sv = 10^6 m^3 s^{-1}). During summer and late fall, we observed Atlantic Water flowing westward (a counter current), north of the common eastward flowing Atlantic Water current. Observations suggest that the counter current is part of a clockwise circulation in the Sofia Deep, north of Svalbard. Our observations also reveal a previously undescribed deep, cold current flowing eastward into the Arctic Ocean. Historical data in the region support the presence of this deep current.

1. Introduction

In a time of decreasing sea ice volume and increasing atmospheric and oceanic temperatures in the Arctic region, understanding the processes controlling the warm water inflow into the Arctic Ocean is becoming increasingly important (Carmack et al., 2015; Polyakov et al., 2017). Relatively warm and salty waters of Atlantic origin (Atlantic Water, AW) enter the Arctic Ocean through the Barents Sea and Fram Strait. The West Spitsbergen current (WSC), located on the eastern continental slope in Fram Strait (Figure 1a), is considered the major oceanic heat source to the Arctic Ocean (Aagaard et al., 1987). However, the AW distribution and circulation in Fram Strait are complex, including multiple branches and recirculation paths (Hattermann et al., 2016; Manley, 1995; Marnela et al., 2013; von Appen et al., 2016).

The outer part of WSC recirculates, joining the East Greenland Current (Hattermann et al., 2016; Marnela et al., 2013; von Appen et al., 2016). Using geostrophic calculations based on summer hydrography, Marnela et al. (2013) found that the recirculation was strongest close to 79°N. Eddy-resolving regional

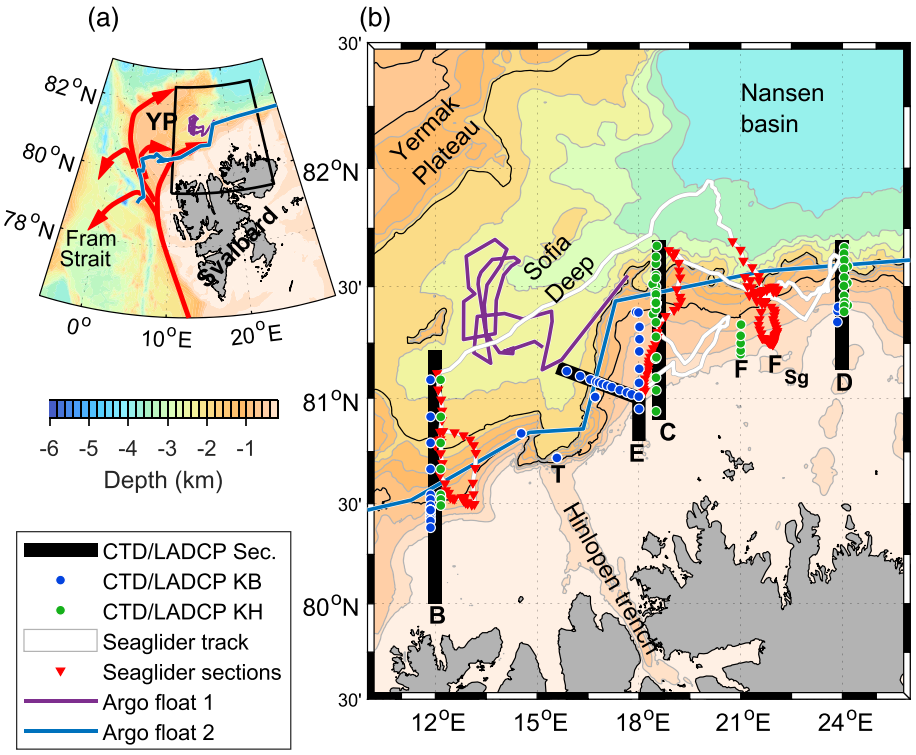

Figure 1. (a) Overview of the region of interest. Red arrows show the Atlantic Water circulation patterns. The black box is enlarged in (b). The Argo float paths are also shown. (b) Observation locations. CTD sections are marked with wide black lines extending from the southern to northern-most CTD profiles. Only CTD stations used for composite sections are marked with circles for clarity (coverage of other stations not shown on the sections can be seen in Figure 2): blue from the RV Kristine Bonnevie (KB) and green from the RV Kronprins Haakon (KH) cruises. Stations occupied in both cruises have been slightly offset for legibility. White line shows the entire Seaglider track, while red triangles show the Seaglider dives used for section plots. Black isobaths are at 800 and 1,500 m. Gray lines are isobaths from 200 to 1,400 m depth at every 200 m, and 2,000 to 6,000 at every 500 m. Letters indicate different sections referred to in the text, except T, which is a repeat occupation of three stations at the slopes of the topographic feature at the mouth of the Hinlopen trench.

ocean model results suggest that this recirculation contains relatively cold AW and is primarily related to the eastern rim of the Greenland Sea gyre, whereas the recirculation of the warmest AW occurs north of 80°N, mainly facilitated by eddies (Hattermann et al., 2016). Near the Yermak Plateau (YP), WSC initially splits into two branches: an outer branch following the slope of the plateau and an inner branch following the edge of the continental shelf, named the Svalbard branch (Aagaard et al., 1987). Further downstream the outer branch again divides into three branches: one branch recirculating in Fram Strait (Bourke et al., 1988; Hattermann et al., 2016; Wekerle et al., 2017), one continuing along the plateau, named the Yermak branch (Aagaard et al., 1987; Cokelet et al., 2008; Perkin & Lewis, 1984), and one flowing over the plateau along a topographic depression, named the Yermak pass branch (Gascard et al., 2013; Koenig et al., 2017; Menze et al., 2019). The Svalbard branch is relatively well-documented and accessible, whereas the outer Yermak and Yermak-pass branches are poorly documented due to meandering currents, challenging sea-ice conditions, and strong seasonal variability (Koenig et al., 2017).

A mooring array maintained across Fram Strait at 79°N shows that the long-term mean transport of waters with potential temperature >2°C in the WSC is about 3 Sv (1 Sv $= 1 \times 10^6$ m^3 s^{-1}) (Beszczynska-Möller et al., 2012). However, the fraction of AW that enters the Arctic Ocean or recirculates westward to join the East Greenland current is not accurately known. As much as 50% of the AW entering Fram Strait is estimated to recirculate (Manley, 1995; Marnela et al., 2013). The Svalbard branch has historically been considered the main AW inflow route to the Arctic Ocean (Aagaard et al., 1987; Cokelet et al., 2008; Perkin & Lewis, 1984), but recent numerical simulations suggest that the Yermak Pass branch can be comparable

(Crews et al., 2019; Koenig et al., 2017). However, in situ observations are needed to quantify the relative contribution and variability of each branch. East of the YP, north of Svalbard, AW volume transport estimates range between 0.5 and 3.4 Sv, depending on the location and time of the observations and the AW definition that is used (Cokelet et al., 2008; Kolås & Fer, 2018; Pérez-Hernández et al., 2017; Våge et al., 2016). The most comprehensive of the estimates in this region is from a year-long record from a 6-mooring array across the continental slope north of Svalbard at 30°E covering the boundary current between the 200 m isobath and 50 km offshore of the shelf break (Pérez-Hernández et al., 2019). Using a definition of AW with potential temperature ≥1°C, practical salinity ≥34.9, and potential density anomaly ≥27.6 kg m^{-3}, the average (±1 standard deviation) AW transport was 2.1 ± 0.2 Sv (Pérez-Hernández et al., 2019). The transport estimates east of the YP likely integrate the contributions from the Svalbard, Yermak pass, and Yermak branches.

The three branches entering the Arctic Ocean are thought to merge and continue as a topographically steered boundary current. The Yermak Pass branch and the Svalbard branch probably merge between 10 and 15°E (Menze et al., 2019). The location where the Yermak branch merges with the other two is not clear. Historical observations suggested that parts of the Yermak branch left the Yermak Plateau at the northeastern tip, crossing over the basin before rejoining the boundary current (Perkin & Lewis, 1984). However, numerical models indicate that the Yermak branch flows around the plateau, following the slope, and rejoin the other branches between 12 and 18°E north of Svalbard (Crews et al., 2018; Koenig et al., 2017). Observations from drifting ice stations during winter and spring 2015 support paths seen in models (Meyer, Sundfjord, Fer, et al., 2017).

As the AW flows toward the Arctic, its hydrographic properties change through atmospheric forcing and interaction with sea ice and surrounding colder and fresher water masses (Boyd & D'Asaro, 1994; Rudels et al., 2000; Onarheim et al., 2014). Over steep topography, strong vertical shear and mixing as well as lateral exchange processes increase the rate of cooling and freshening. At the latitudes of YP, the along-path cooling and freshening is estimated to be 0.2°C per 100 km and 0.01 g/kg per 100 km, respectively, corresponding to a surface heat flux between 400 and 500 W m^{-2} (Boyd & D'Asaro, 1994; Cokelet et al., 2008; Saloranta & Haugan, 2004; Kolås & Fer, 2018). Such heat fluxes are much larger than the turbulent heat fluxes commonly observed near the YP. Typical heat fluxes near the plateau are $\mathcal{O}(10)$ W m^{-2}, and episodic events may reach $\mathcal{O}(100)$ W m^{-2} (Fer et al., 2010; Meyer, Fer, et al., 2017; Sirevaag & Fer, 2009). It is not clear which processes can sustain such along-path cooling rates; however, eddies are thought to play a major role in this heat loss (Crews et al., 2019; Kolås & Fer, 2018; Våge et al., 2016). Eastward of 20°E, observations suggest substantially less along-path cooling (Pérez-Hernández et al., 2017).

In this study, we use observations during summer and fall 2018 (Figure 1b) to obtain a detailed description of the AW boundary current structure and volume transport north of Svalbard, east of the Yermak Plateau, and to quantify the intraseasonal variability. Our analysis identifies previously unknown circulation patterns in the region which may have implications for the transport and variability of the AW.

2. Data

Observational data from two scientific cruises (Fer et al., 2019, 2020), carried out as a part of the Nansen Legacy project, are supplemented by one Seaglider mission (Kolås & Fer, 2020) and two Argo floats north of Svalbard. All data were collected between July and December 2018. Station locations and tracks are shown in Figure 1b, and platform specific details are given in the corresponding subsections below.

2.1. Hydrographic Measurements From Cruises

The cruises were conducted by the Research Vessel (RV) Kristine Bonnevie between 27 June and 10 July 2018 and by the RV Kronprins Haakon between 12 and 24 September 2018. CTD profiles during both cruises were collected using a Sea-Bird Scientific, SBE 911plus system, with a 200 kHz Benthos altimeter allowing measurements close to seabed; 120 and 160 CTD profiles were collected during the summer and fall cruises, respectively. Water samples drawn at each station were used to calibrate salinity and dissolved oxygen measurements. Pressure, temperature, and practical salinity data are accurate to ±0.5 dbar, $\pm 2 \times 10^{-3}$°C, and $\pm 3 \times 10^{-3}$, respectively. CTD data were processed using the standard SBE Data Processing software. Conservative Temparature, Θ, and Absolute Salinity, S_A, were calculated using the thermodynamic

equation of seawater (IOC et al., 2010), and the Gibbs SeaWater Oceanographic Toolbox (McDougall & Barker, 2011).

2.2. Current Profiles From Cruises

The CTD frames on both vessels were fitted with a pair of acoustic Doppler current profilers (ADCPs), so-called lowered-ADCPs (LADCPs). The LADCPs were 6,000 m-rated 300 kHz Teledyne RD Instruments (RDI) Sentinel Workhorses, one mounted pointing downward and one upward. The LADCPs were synchronized and set to provide data vertically averaged in 8 m bins. On the Kristine Bonnevie the LADCPs had internal batteries, while on the Kronprins Haakon they had an external battery mounted on the frame. Compasses were calibrated on land prior to cruises with resulting errors less than 1–2°. LADCP data were processed using the LDEO software version IX-13 based on Visbeck (2002). The LADCP profiles were constrained by navigation data and 5-min averaged profiles from the ship's ADCPs (SADCP).

RV Kronprins Haakon had four SADCPs: two 38 kHz and two 150 kHz Teledyne RDI Ocean Surveyors. One of each was mounted on a drop keel, and one of each was flush-mounted in the hull. Flush-mounted ADCPs were protected by an acoustically transparent window allowing for profiling when moving through ice. Only the 38 kHz ADCP mounted on the drop keel was used for constraining the LADCP processing. Kristine Bonnevie had a 150 kHz Teledyne RDI Ocean Surveyor SADCP. The ADCPs collected profiles in 8 m vertical bins below a blank distance of 16 m. The data were collected using the VmDAS software onboard Kronprins Haakon and the UHDAS software onboard Kristine Bonnevie. Horizontal velocity profiles were obtained as 5 min averages using the University of Hawaii postprocessing software, to an uncertainty of 2–3 cm s^{-1} (Firing & Ranada, 1995).

2.3. Seaglider Data

A Kongsberg Seaglider was deployed from the RV Kronprins Haakon on 17 September 2018. The Seaglider track (Figure 1b) was planned to maximize the number of cross-sections along the boundary current, while avoiding sea ice. A total of 377 dives (754 profiles) were performed before recovery on 11 November 2018. The typical horizontal distance between two surfacing locations was 3 km. The Seaglider operated between the surface and 1,000 m depth, sampling CTD on both dives and climbs at a sampling rate of 10 s in the upper 200 m, 20 s between 200 and 600 m, and 30 s below 600 m. The vertical velocity was normally close to 10 cm s^{-1}. For each dive, a depth-averaged current (DAC) is estimated based on the deviation between expected surfacing location deduced from the flight model and the actual surfacing location. The Seaglider was equipped with a Paine strain-gauge pressure sensor, a SBE CT Sail and an Aanderaa dissolved oxygen sensor. The data set was processed using the University of East Anglia Seaglider toolbox (http://www.byqueste.com/toolbox.html), based on the methods described by Garau et al. (2011) and Frajka-Williams et al. (2011). Processed S_A and Θ are accurate to 0.01 g kg^{-1} and 0.001°C, respectively, and DAC is accurate to 0.01 m s^{-1} (p. 9 "Seaglider Quality Control Manual," 2012). Data spikes above three standard deviations, for each pressure level over all profiles, were removed during postprocessing. Finally, a salinity offset correction of 0.005 g kg^{-1} was applied after comparing the deep part of Seaglider dives (750 to 1,000 m) to nearby CTD profiles (within 7 days and 15 km) collected from the RV Kronprins Haakon.

2.4. Argo Floats

Current trajectories from two Argo floats, WMO Id 6903548 and 3901910, hereby referred to as float 1 and 2, were available north of Svalbard in the period from June to December 2018. Both floats drifted at a parking depth of 1,000 dbar, profiling between a maximum depth of 2,000 dbar and the surface. Float 1 profiled every 3 days from June to 9 November, and every 10 days thereafter, and float 2 every 7 days during the study period. We calculated the current trajectories at 1,000 m depth at the midposition between two surfacing locations by dividing displacement by time. The Argo float data were collected and made freely available by the International Argo Program and the national programs that contribute to it (http://www.argo.ucsd.edu, http://argo.jcommops.org) (International Argo Program, 2003). The Argo Program is part of the Global Ocean Observing System.

2.5. NORA10

Wind speed and direction at 10 m above sea level were extracted at hourly intervals in the area north of Svalbard (0–35°E, 79°N–83°N), from the Norwegian Reanalysis Archive (NORA10; Reistad et al., 2011).

NORA10 is a regional high resolution (10–11 km) atmospheric downscaling of ERA-40 (Uppala et al., 2005) and ECMWF IFS (European Center for Medium-Range Weather Forecasts Integrated Forecasting System) operational analyses (after 2002), covering the northern North Atlantic and the Barents Sea. The dynamic atmospheric downscaling is performed as a series of short prognostic runs (using High Resolution Limited Area Model) initialized from a blend of ERA-40 and the previous prognostic run to preserve the fine-scale surface features from the high-resolution model, while maintaining the large-scale synoptic field from ERA-40. We calculated the wind stress components, using the Large and Pond (1981) parameterization, and the wind stress curl over the region of interest (box in Figure 8c). We present time series spatially averaged over the region and time-averaged fields during cruise periods and Seaglider transects.

2.6. Historical Data

Historical data for the region around Svalbard were obtained from the UNIS hydrographic database described by Skogseth et al. (2019). We used a subset of these data covering the continental slope north of Svalbard between 12°E and 24°E, for the months July to November. The profiles were initially scanned visually to remove large spikes, before removing data above three standard deviations at each pressure level over all profiles. A total of 1,118 profiles were used for the composite section (section 4.7), 65% of these were collected pre-2008 and 35% in the last decade.

2.7. Other Data Sets

Barotropic tidal currents were obtained from the Arctic Ocean Inverse Tide Model on a 5 km horizontal grid (Arc5km2018) (Erofeeva & Egbert, 2020). We used the eight main constituents (M_2, S_2, N_2, K_2, K_1, O_1, P_1, and Q_1) and four nonlinear components (M_4, MS_4, MN_2, and $2N_2$), to predict the horizontal tidal volume transport ($m^2\ s^{-1}$) at profile location and midtime for cruise stations and at time and location of the Seaglider calculated from a flight model.

Bathymetry data are from the third version of the International Bathymetric Chart of the Arctic Ocean (IBCAO) (Jakobsson et al., 2012). We used the 30 arc-seconds grid in our analysis.

Daily mean sea ice properties based on satellite observations at 10 km grid resolution are obtained from the EUMETSAT Ocean and Sea Ice Satellite Application Facility (OSI SAF, www.osi-saf.org).

3. Methods

3.1. Detiding Current Measurements

Current profile measurements from LADCPs and SADCPs and the DAC from the Seaglider were detided using the Arc5km2018 inverse tidal model. Barotropic tidal currents were obtained by dividing the predicted barotropic tidal transport at the time and location of the measurement, by the total water depth at measurement location. Water depth at measurement location was interpolated from a smoothed version of IBCAO (described in section 3.3). The barotropic tidal components were subtracted from the measured currents.

Detiding of the DAC measured by the Seaglider needs care because one dive-climb cycle takes about 6 hr (time between pairs of predive and postclimb GPS fixes). We estimated the average tidal current during the dive-climb cycle. Based on the Seaglider flight model, latitude, longitude, and time stamps were estimated for every decibar during the dive-climb cycle. These values were used as input to predict the barotropic tidal transport at given time and location at each depth level. Bottom depth along the Seaglider track was interpolated from the smoothed IBCAO field, in order to obtain tidal velocity. Finally, we calculated the average tidal current during profiling and subtracted it from the Seaglider's depth average current.

3.2. Synoptic Sections

Each section (section B, C, D, E, and F, see Figure 1) is defined along a line normal to the 800 m isobath close to the original station locations. Note that the stations identified with markers in Figure 1 are for those used to construct composites (section 3.3), and the complete station coverage along each section can be seen (arrowheads) in Figure 2. Using station depth obtained from the smoothed IBCAO field, we moved each station along isobaths onto the corresponding section. The current vectors u and v (east and north) were rotated to obtain along isobath velocity u_r (>0 eastward) and across isobath velocity v_r (>0 toward deep water), relative to the local 800 m isobath's orientation at the corresponding section. Distance to the 800 m isobath is positive toward the shelf and negative toward deep waters. Seaglider data were horizontally averaged in

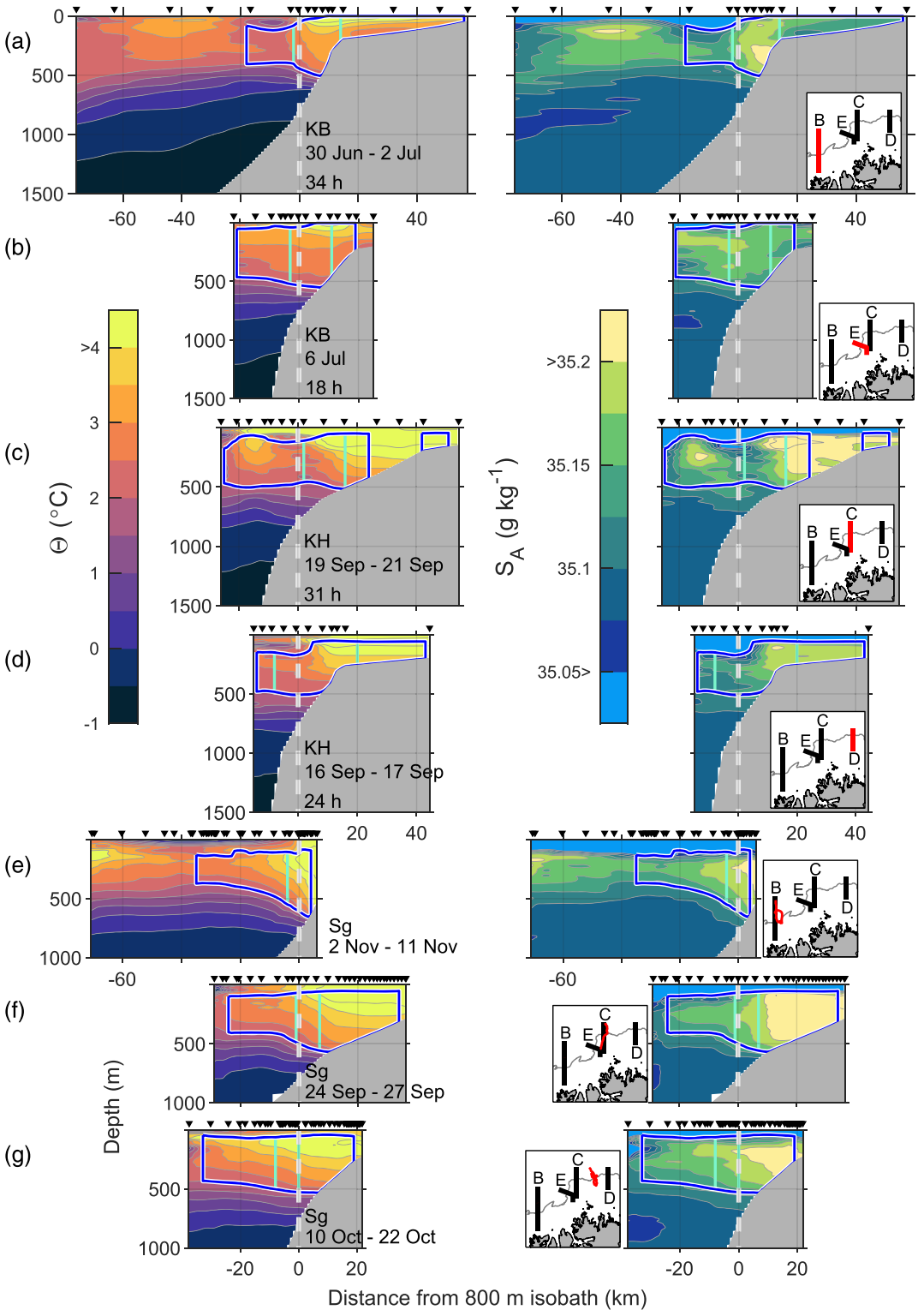

Figure 2. Conservative Temperature, Θ, and Absolute Salinity, S_A, for synoptic sections. The section displayed in each row is indicated by a red line in the respective overview inset on the right. The white dashed line at 0 km and the isobath marked in the overview inset show the location of the 800 m isobath. Blue line envelopes AW with $U_g > 0$. Green vertical lines envelope the stream tube used in the along-path heat loss calculations. Black triangles at the top of each panel show cruise profile location and Seaglider surface location. KB = RV Kristine Bonnevie, KH = RV Kronprins Haakon, Sg = Seaglider.

2 km bins before interpolation. All sections, including the Seaglider sections (B_{sg}, C_{sg}, and F_{sg}), were interpolated onto a 2 m × 1 km grid (vertical × horizontal). We used a Laplacian spline interpolation method with tension, choosing a 15 km search radius and no smoothing (Smith & Wessel, 1990; Pickart & Smethie, 1998). Finally all sections are smoothed using a 20 m × 20 km moving average window to remove small scale variability.

3.3. Composite Sections

Composite sections for each cruise and the Seaglider were constructed by organizing the data on the average bathymetry profile described in Appendix A. A station is positioned at the distance on the average bathymetry profile corresponding to the water depth at measurement location. After locating each station at the cross section, the data were binned, interpolated, and smoothed similar to the synoptic sections described in section 3.2. CTD stations used for the summer and fall composite sections are shown in Figure 1. All Seaglider dives were included in the late fall composite.

Prior to generating the composite section, velocity vectors are projected onto local along- (u_r) and across-isobath (v_r) components using the smoothed IBCAO bathymetry to remove small scale local variations in topographic gradients. Smoothing is made using a 3 km Gaussian window as a 2-D convolution operator. The bathymetry gradients at each CTD station and average Seaglider dive locations were then used to project velocity vectors onto along- and across-isobath vectors. The along-isobath component of the de-tided observed velocity in these composite sections is used to constrain the geostrophic velocities (section 3.4).

3.4. Absolute Geostrophic Velocity and Atlantic Water Volume Transport

Relative geostrophic velocity was obtained from Gibbs SeaWater Oceanographic Toolbox using dynamic height anomaly referenced to the surface pressure (McDougall & Barker, 2011). Absolute geostrophic velocities were obtained by vertically integrating the geostrophic shear and constraining its depth average by the along-isobath component of the observed depth-averaged current. For sections B, C, E, D, and the composite sections, the observed depth-averaged current was obtained from LADCPs, whereas for the synoptic and composite Seaglider sections DAC was used.

We calculated the transport density U_g ($m^2\ s^{-1}$) in the AW layer by vertical trapezoidal integral of the geostrophic current u_g. Following Swift and Aagaard (1981), Aagaard et al. (1985) and Cokelet et al. (2008), we defined AW as water with $\Theta > 2°C$ and $S_A > 35.05\ g\ kg^{-1}$. Lateral boundaries of the AW inflow were defined as the location where the layer integrated velocity was zero ($U_g = 0$). Total volume transport was then computed as the horizontal integral of $U_g > 0$.

3.5. Along-Path Rate of Change of Heat Content

We estimate the along-path heat loss of the AW inflow by comparing the integrated heat content of AW from one cross-slope section to the next further downstream. As shown in IOC et al. (2010) and McDougall (2003) the first law of thermodynamics is practically equivalent to the conservation equation for Conservative Temperature (Θ), which is proportional to potential enthalpy, h_0, as $\Theta = h_0/C_p$. The heat content per unit mass of seawater is then $C_p\Theta$, where $C_p = 3991.867\ J\ kg^{-1}\ K^{-1}$ is the specific heat (IOC et al., 2010). Finally, heat content is integrated laterally and vertically in the cross-slope region, to obtain total heat content per downstream meter.

While the AW volume transport for each section can be calculated as described in section 3.4, the calculation of the heat loss between sections using the rate of change in heat content requires that the volume transport is conserved. For each synoptic section, we therefore defined a stream tube conserving a specified volume transport of AW, representative of the core of the current. We constrained each stream tube at 1.1 Sv, which is the AW volume transport through section D after excluding the outer parts with station gaps. Starting at the location of maximum layer-integrated velocity (i.e., maximum U_g), we integrated U_g symmetrically across the section until we reached the target volume transport. For each stream tube we calculated velocity-weighted average Θ and S_A, and average u_r.

The along-path rate of change of heat content calculation is based on the methods described by Boyd and D'Asaro (1994) and Cokelet et al. (2008), assuming only the eddy fluxes at the surface are important and neglecting thermal inertia and local advection of heat. Then all observed heat loss, Q, must be due to heat

fluxes through the surface of our stream tubes. Applying Gauss theorem on the volume integral of the heat advection yields

$$\int_{Surface} Q dxdy = \rho_0 C_P \overline{u} \int_A \frac{\partial \Theta}{\partial y} dxdz, \quad (1)$$

where the area integral is taken over the stream tube's cross section A, $\overline{u}$ is the mean u_r (along-isobath velocity), and ρ_0 is the reference seawater density. Here, y is the along-path coordinate and estimated as the distance between the sections along the 800-m isobath north of Svalbard. The along-path temperature gradient was obtained from the slope of a line fit to along-path distance against the velocity-weighted average Θ for each section. The advected area-integrated heat content change per along-path meter (W m^{-1}) from Equation 1 was divided by the average width of the stream tube to obtain the surface heat flux (W m^{-2}). These calculations are similar to and can be compared with those reported in Kolås and Fer (2018) for the AW current west of Spitsbergen.

4. Results

The summer, fall, and late fall conditions are presented, first in form of individual sections and then the corresponding composite sections. Figure 2 shows Conservative Temperature (Θ) and Absolute Salinity (S_A) for sections B, C, D, and E, and Seaglider sections B_{Sg}, C_{Sg}, and F_{Sg}. Figure 3 shows the same synoptic sections as Figure 2 but for absolute geostrophic velocity. Figure 4shows the composite sections for the summer cruise, fall cruise, and the Seaglider mission (late fall).

4.1. Summer

Sections B and E were collected during June and July from the RV Kristine Bonnevie and are referred to as the summer sections (Figures 2a, 2b, 3a, and 3b). Section B shows two cores in Θ and S_A. The outer core is located at −40 km, roughly above the 1,700 m isobath, while the inner core is located at 10 km. The inner core is the AW boundary current flowing eastward into the Arctic and transports 1.8 Sv of AW. Details are given in Table 1. Four days later at section E the transport is 1.7 Sv. Section E does not capture the outer extent of the AW, however, covers its dynamic core. While the average AW salinity remains roughly the same from B to E, the temperature decreases slightly by 0.2°C. The upper layer of AW is known to enter the Hinlopen trench at 17°E (Figure 1) and is likely cooled as a result of this circulation (Menze et al., 2019). The maximum AW temperature is found near the surface in both sections. In section B, there is a clear salinity maximum near the seabed at the shelf break (right panel of Figure 2a), which is absent in section E. A likely explanation for this is convectively driven mixing induced by downslope Ekman transport advecting lighter water under denser water, known to be important in the region (Kolås & Fer, 2018).

The along-path rate of change of heat content advected in the AW layer from sections B to E is -9.1×10^7 W m^{-1}, corresponding to a heat loss of 550 W m^{-2}. Note that at this section the temperatures are increasing toward the surface; thus any heat loss must be caused by lateral mixing or advection or by vertical mixing with colder waters below the Atlantic layer. However, there may be upward heat loss to the overlying waters on the shelf as the AW circulates in the Hinlopen trench. AW heat loss in the Hinlopen trench has not been accounted for when calculating heat loss along the 800 m isobath. The along-path temperature and salinity gradients are −0.21°C/100 km and −0.015 g kg^{-1}/100 km, respectively, from sections B to E.

The summer composite hydrography shows a two-branch structure in temperature and salinity (Figures 4a and 4b), where the outer branch flows westward and the inner branch eastward (Figure 4c). The inner branch is barotropic and symmetrically centered around 8 km. In summer, the average AW transport into the Arctic is 2.0 Sv. The outer branch, located at −30 km, is baroclinic, with eastward bottom currents. Possible origin of this bottom-intensified current will be discussed in section 5.3. Geostrophic velocity integrated vertically over the AW layer shows a weak westward AW transport in the outer branch (Figure 4d). This westward transport is consistent in all our composite sections and motivated us to calculate the general statistics of this flow (see Table 2). The average temperature of the reverse current is 0.4 to 0.9°C lower than the main branch.

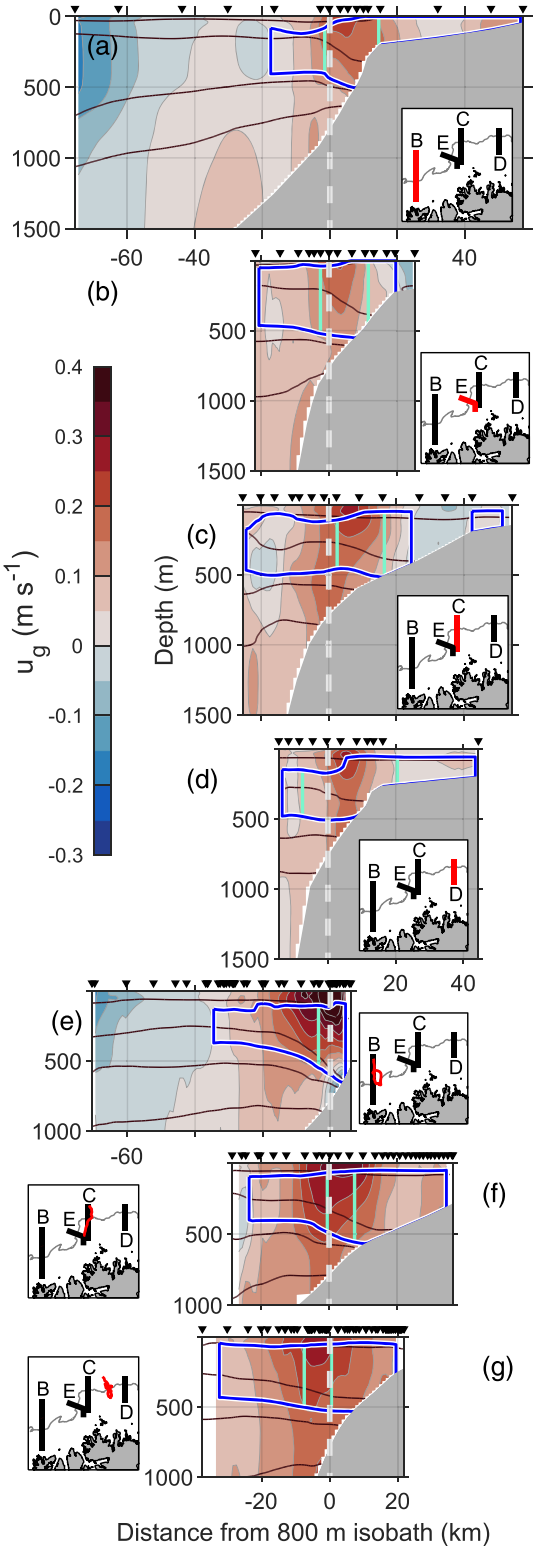

Figure 3. Same as Figure 2, but for along-isobath absolute geostrophic velocity, u_g. Black lines are σ_0 contours. Positive velocities are approximately eastward along the continental slope.

4.2. Fall

Figures 2c and 2d show sections C and D during the September cruise. Section C shows two separate cores in Θ and S_A, an outer core located at −15 km, and an inner core near the 500 m isobath at 20 km. u_g does not show the same two-core structure (Figure 3c) but a surface-intensified core with a vertically integrated u_g maximum at 9 km. However, the isopycnals spread roughly where the outer core is located and u_g becomes negative. This suggests that the outer core may be water trapped in an anticyclonic eddy, detached from the inner core, with a center at the edge of section C. The AW volume transport at section C is 1.9 Sv (Table 1). Note that an opposing flow between 22 and 41 km on the shelf, where u_g is negative, divides the AW layer.

Section D at 24°E, conducted 4 days prior to section C, shows a less saline AW layer, indicating mixing with surrounding fresher water masses. Θ and S_A maxima are located at the shelf break, while the u_g core is located above the 550 m isobath (Figure 3d). Section D shows a sharp front between AW and polar surface water with polar surface water intruding above the outer part of the AW layer. Note the large gap without stations between 20 and 40 km on the shelf. The AW volume transport at section D is 1.4 Sv.

The along-path rate of change of heat content advected from section C to D is -9.6×10^6 W m^{-1}, equivalent to a surface heat loss of 420 W m^{-2}. The along-path temperature and salinity gradients are −0.21°C/100 km and −0.017 g kg^{-1}/100 km, respectively.

The middle column of Figure 4 shows the composite section from the September cruise. The AW layer flowing into the Arctic is wide with two salinity cores (Figure 4b). The outer core is co-located with a local u_g maximum (Figure 4c), also observed as a peak in U_g (Figure 4d). The transport estimated from this composite is 2.9 Sv, larger than that in the synoptic sections C and D (1.9 and 1.4 Sv, respectively). One reason for this is that the composite section contains more CTD stations (along 12°E and 21°E, see Figure 1b) than only those from the two synoptic sections. In addition, the counter current observed on the shelf in section C is missing in the composite, thus increasing the cross-stream area of the eastward flow. However, although the composite sections are useful, allowing direct comparison between cruises, we do alter the cross-stream Θ and S_A gradients by moving stations onto corresponding isobaths on the composite section. This can potentially lead to unrealistic u_g estimates, which we discuss in section 5.4.

4.3. Late Fall

Figures 2e–2g show the Seaglider sections conducted between late September and early November. Section B_{Sg} (Figure 2e) is at the same location as section B. Of the two cores of warm and saline AW seen in the Θ and S_A distribution, only the inner branch is the eastward flowing boundary current (Figure 3e). The outer branch, starting at −40 km, flows westward and is surface intensified. The AW transport at section B_{Sg} is 2.3 Sv; however, this transport is likely an underestimate because the shallow side of the AW layer on the shelf is not captured by the Seaglider.

Section C_{Sg} (Figures 2f and 3f) is at the same location as section C. Whereas both the Θ and S_A maxima are located up-slope of the 800 m

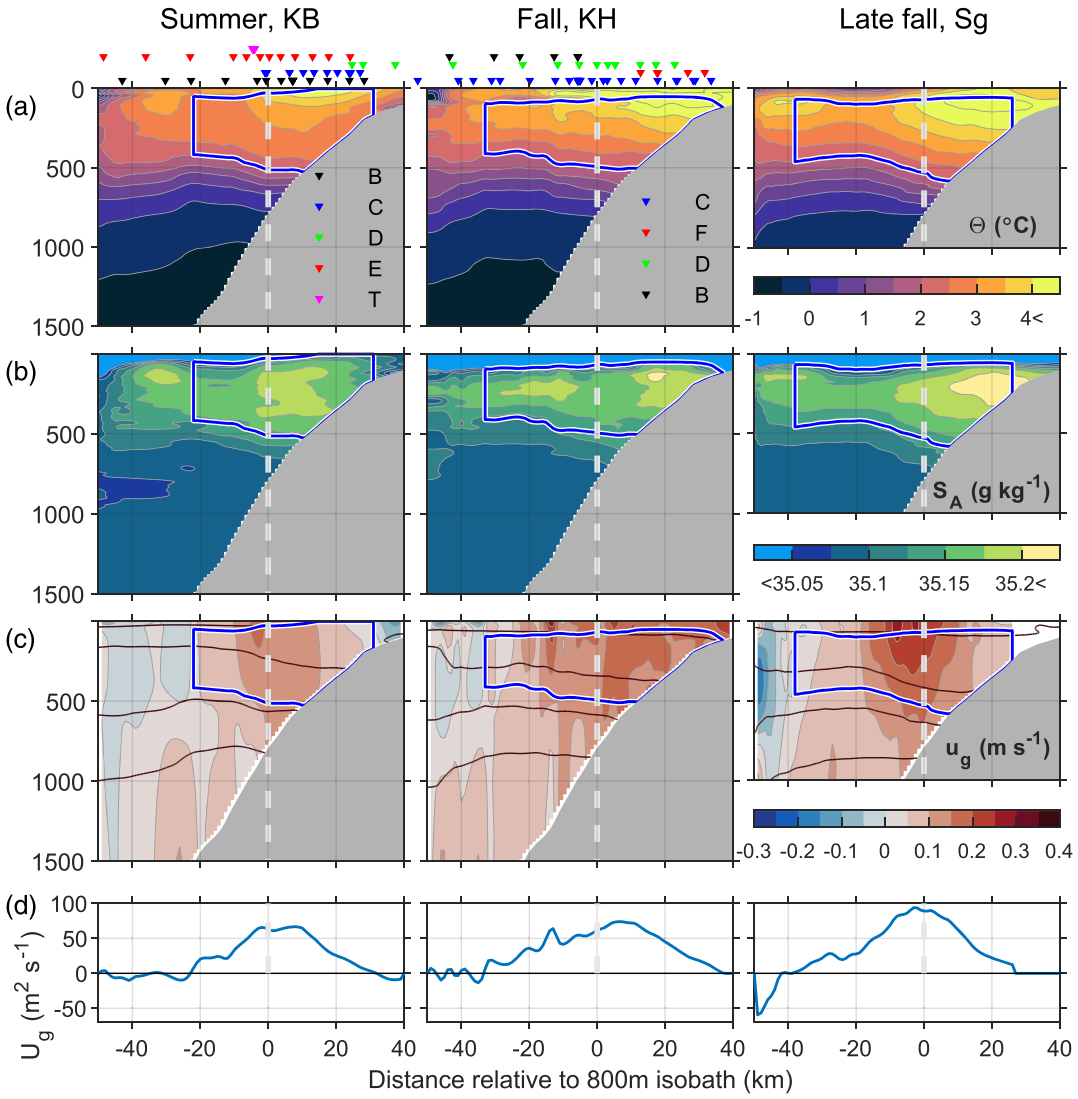

Figure 4. Composite sections for the summer cruise (KB), the fall cruise (KH), and the Seaglider mission during late fall (Sg). White dashed line at 0 km indicates the location of the 800 m isobath. Arrowheads, colored for the sections as indicated, show the location of the profiles. (a) Conservative Temperature, Θ, (b) Absolute Salinity, (c) along-isobath absolute geostrophic velocity, u_g, and (d) transport density, U_g, calculated by vertically integrating u_g within the Atlantic Water layer defined by temperature and salinity properties. Blue line envelopes the Atlantic Water with $U_g > 0$ used in transport calculations.

isobath, the u_g core is located at the 800 m isobath. The AW volume transport is 3.5 Sv. Note that section C_{Sg} was conducted only a few days after section C, where the AW volume transport was 1.9 Sv. The large increase from section C to C_{Sg} will be discussed in section 5.2.

Finally, section F_{Sg} (Figures 2g and 3g) is located between C and D. Section F_{Sg} is very similar to section C_{Sg}. Θ and S_A cores are located up-slope from the u_g core, and the AW transport is 3.4 Sv.

While conserving the volume transport in stream tubes (as described in section 3.5) we calculated the along-path rate of change of heat content advected from section B_{Sg} to F_{Sg} to be -1.5×10^7 W m^{-1}, where the temperature gradient was −0.34 °C/100 km. For comparison, Saloranta and Haugan (2004) found a downstream winter temperature gradient of −0.34 °C/100 km west of Svalbard. Due to the large time difference between the Seaglider sections we had to account for the seasonal temperature change. Using a linear fit to the mean AW stream tube temperatures and time of occupations of sections B, C, C_{Sg}, and B_{Sg} we found a

Table 1
Properties of the Atlantic Water Boundary Current

Section	$\overline{\Theta}$ (°C)	$\overline{S_A}$ (g kg^{-1})	$\overline{u_g}$ (m s^{-1})	Area (km^2)	Transport (Sv)
B	3.2 ±0.1	35.16 ±0.01	0.10	17	1.8 ±0.1
E	3.0 ±0.1	35.16 ±0.01	0.09	18	1.7 ±0.1
C	3.1 ±0.1	35.15 ±0.01	0.08	26	1.9 ±0.1
D	3.2 ±0.1	35.14 ±0.01	0.08	15	1.4 ±0.2
B_{Sg}	3.5 ±0.1	35.16 ±0.01	0.15	13	2.3 ±0.1
C_{Sg}	3.4 ±0.1	35.17 ±0.01	0.15	22	3.5 ±0.1
F_{Sg}	3.4 ±0.1	35.16 ±0.02	0.16	21	3.4 ±0.2
Summer	2.9 ±0.1	35.16 ±0.01	0.09	21	2.0 ±0.1
Fall	3.3 ±0.1	35.16 ±0.02	0.13	23	2.9 ±0.4
Late fall	3.3 ±0.1	35.16 ±0.01	0.11	25	3.0 ±0.2
Average	3.2 ±0.1	35.16 ±0.01	0.10	25	2.6 ±0.2

Note. Calculations are presented for the synoptic sections, the seasonal composite sections, and the full period average composite section. For calculation methods the reader is referred to section 3. Overbar denotes velocity-weighted arithmetic means. Error calculations are described in Appendix B and are rounded to one significant digit for Θ and volume transport and two significant digits for S_A.

seasonal change of 0.20°C/month. A linear fit approximates the segment of the annual cycle between July and November well. Note that before applying the linear fit, the average stream tube temperatures in sections C and C_{Sg} were moved to section B location by using the downstream temperature gradient observed during summer and fall. This was done in order to minimize the spatial contribution in the seasonal change estimate.

Similar to the summer section, the composite section obtained from all data collected by the Seaglider shows a two-branched structure in Θ and S_A, where the outer branch flows westward (the right column of Figure 4). The inner branch (marked with blue box) is the boundary current flowing into the Arctic. u_g and U_g are centered at the 800 m isobath. The AW transport estimate is 3.0 Sv.

4.4. Average Section

An average section is obtained by averaging the summer, fall, and late fall composites for Θ and S_A (Figure 5). Relative geostrophic velocity is then calculated from the average Θ and S_A fields (Figure 5a), and absolute geostrophic velocity is obtained by using the average 0–1,000 m depth-averaged observed velocity from all three data sets as reference velocity. That is, we calculate the 0–1,000 m depth-averaged LADCP velocity from the composite of the along-isobath component of the summer and fall cruises and finally average the depth-averaged currents together with the Seaglider DAC. We use the 0–1,000 m depth-averaged current to be consistent with the Seaglider which averages the currents in the upper 1,000 m. However, the results are not sensitive to this: When compared to the full depth averages, LADCP 0–1,000 m average current differed by less than 0.5 cm s^{-1}.

Two branches identified by temperature and salinity maxima separate at the 1,500 m isobath (−20 km), where the isopycnals shoal locally. The inner branch is the AW boundary current with an average volume transport of 2.6 Sv. The outer branch is a westward current that transports about 0.1 Sv of AW (see Table 2 for details). We note that the westward flowing branch is not fully captured by our observations, and our calculations are potentially an underestimate. The two branches, each about 500 m thick, are separated by a thinner AW layer. Figures 5b–5d show the summer, fall, and late fall anomalies, respectively. Anomalies, calculated by subtracting the seasonal average from the individual composites, highlight the changes that occurred from summer through late fall. During summer, the AW is characterized by negative salinity and temperature anomalies, overlain by a relatively salty surface layer. Throughout the summer and fall, the surface layer freshens because of summer sea ice melt, and the AW becomes warmer and saltier. From fall to late fall the surface layer above the AW cools and the salinity increases again, while the Atlantic layer continues to heat and increase in salinity, especially at depth. The outer branch shows an even stronger seasonal change than the inner branch, suggesting more AW is directed into the outer branch during late fall.

Between summer and late fall, we observe a 1 ±0.3 Sv increase in the AW inflow, with maximum transports observed during October. In the same period, the velocity-weighted average AW temperature increased by 0.4 ±0.2°C. The seasonal increase in transport and heat content of the Atlantic Water Boundary current can be linked to the seasonal variability of the Atlantic Water inflow west of Svalbard, which is known to be at a maximum at the end of fall/beginning of winter (Beszczynska-Möller et al., 2012).

From the u_g anomalies we see that the current intensifies from summer to fall, as its core shifts seaward. Below the AW layer, there is an outer bottom-intensified current, which we discuss in section 5.3. The bottom-intensified current is capped by a local salinity minimum shown with the red contour in the S_A plot. This salinity minimum is common in the Eurasian Basin and is identified as the Arctic Intermediate Water formed in the Nordic Seas (Rudels et al., 2005).

Table 2
Properties of the Atlantic Water Reverse Current (U_g< 0)

Section	$\overline{\Theta}$ (°C)	$\overline{S_A}$ (g kg^{-1})	$\overline{u_g}$ (m s^{-1})	Area (km^2)	Transport (Sv)
Summer	2.5	35.14	0.01	10	−0.1
Fall	2.6	35.14	0.02	5	−0.1
Late fall	2.7	35.14	0.08	4	−0.2
Average	2.3	35.13	0.02	3	−0.1

Note. Calculations are presented for the seasonal composite sections and the full period average composite section. Overbar denotes velocity-weighted arithmetic means. The negative transports are westward.

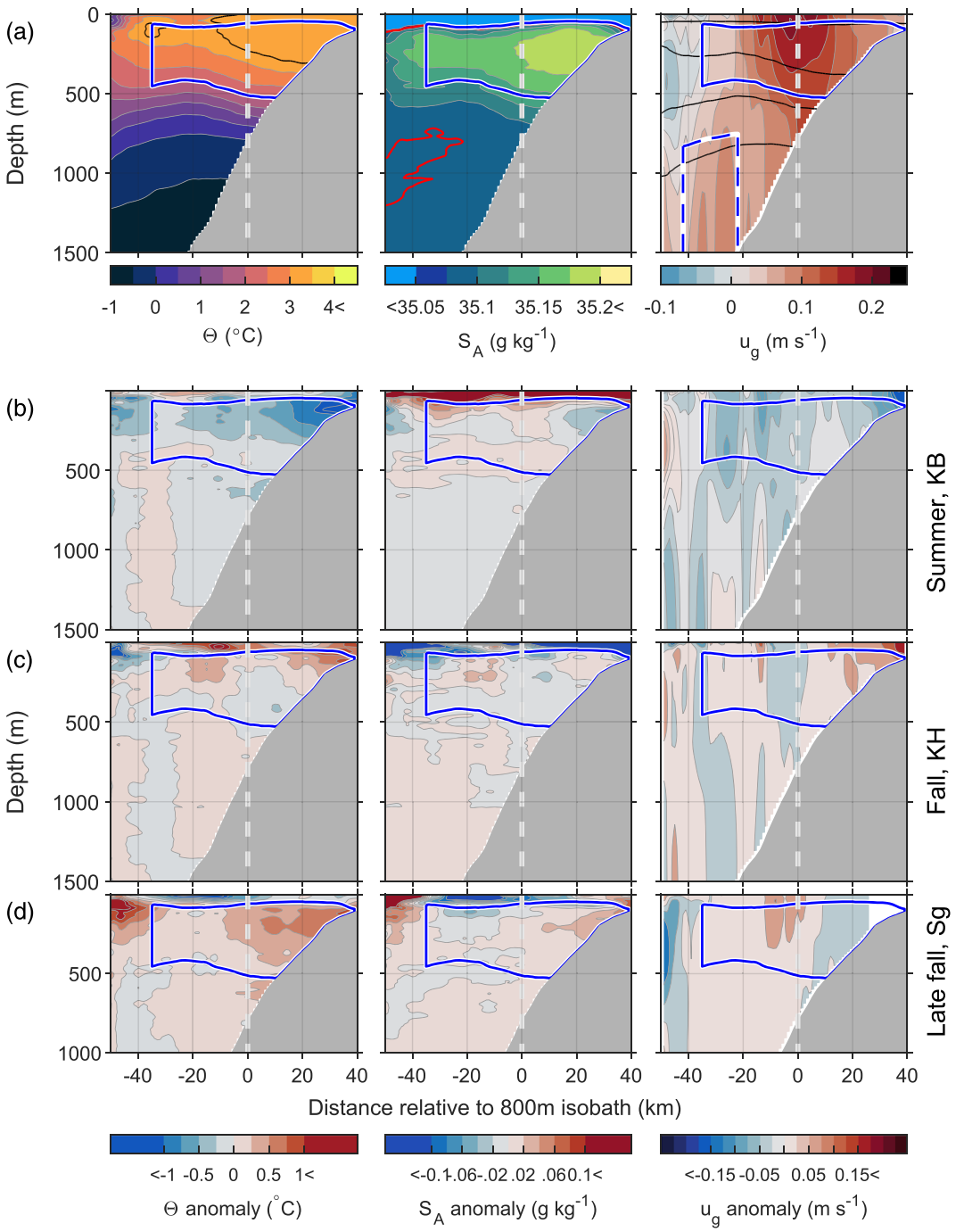

Figure 5. (a) Average composite sections for Θ, S_A, and u_g, based on the summer, fall, and late fall composites in Figure 4. Anomalies for Θ, S_A and u_g from the average composite section are shown for (b) summer, (c) fall, and (d) late fall. White dashed line indicates the location of the 800 m isobath. Blue line envelops the Atlantic Water with $U_g > 0$. Blue dashed line envelopes the bottom-intensified current. Black line in the Θ plot is the 3.3°C isotherm. Red line in the S_A plot is the 35.08 g kg^{-1} isohaline. Black lines in the u_g plot are isopycnals.

In our study period, we identify two main domains on $\Theta - S_A$ space, where water flows into the Arctic Ocean (Figure 6). We compute the volume transport from the composite section using bins of $d\Theta = 0.25$°C and $dS_A = 0.01$ g kg^{-1}. The transport is concentrated in the boundary current transporting AW (2.6 Sv), and the bottom-intensified current transporting Arctic Intermediate Water, Eurasian Basin Deep Water, and

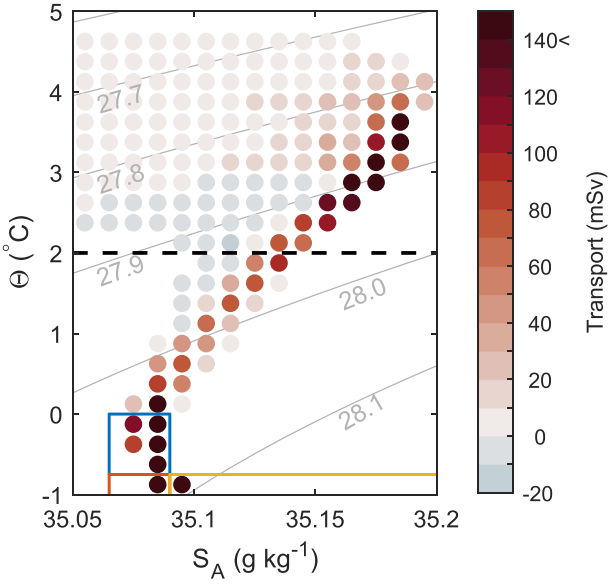

Figure 6. $\Theta - S_A$ diagram from the seasonal average composite section (Figure 5), showing volume transport estimated for $\Theta - S_A$ grid cells ($dS_A = 0.01$ g kg^{-1}, $d\Theta = 0.25$°C). Blue box encloses Arctic Intermediate Water, red encloses cold Norwegian Sea Deep Water, and yellow encloses Eurasian Basin Deep Water (Schlichtholz & Houssais, 2002). Black dashed line indicates the lower Θ boundary of the Atlantic Water.

cold Norwegian Sea Deep Water (water mass definitions from Schlichtholz and Houssais (2002)). In order to quantify the contribution from the bottom-intensified current, we excluded water masses with $\Theta > 0$ and $S_A > 35.1$ and integrated u_g vertically to obtain layer-integrated velocity. The lateral boundaries were set where the layer-integrated velocity first reduced to less than 50% of its maximum. This yielded the blue dashed line enveloping the bottom-intensified current in the u_g plot in Figure 5a. Transport by the bottom-intensified current is 1.5 Sv and represent 35% of the observed flow entering the Arctic Ocean. The average temperature and salinity are −0.6°C and 35.08 g kg^{-1}, respectively, with an average geostrophic velocity of 0.07 m s^{-1}.

4.5. Vertically-Averaged Currents

Circulation patterns inferred by combining all our measurements can help interpret the hydrographic observations. Figure 7a shows observed average currents between June and November, while Figure 7b shows the objectively mapped field of the average currents. The average circulation during our study period is obtained using observations from LADCPs, SADCPs, and the DAC from the Seaglider. Observations were averaged over the upper 1,000 m (or full depth if shallower), before bin averaging in 3 km by 3 km horizontal bins. Average currents were objectively interpolated using a covariance function depending on the spatial distance between binned observations and the fractional distance to large-scale barotropic potential vorticity (f/H) contours (Böhme & Send, 2005). We used a 25 km correlation length scale, based on the semivariogram analysis described in Appendix B and 20% error. Currents from Argo floats were calculated from the displacement between two surfacing locations; however, they were not included in the objective interpolation as their drift at 1,000 m depth may not be representative of the upper 1,000 m average currents.

The AW boundary current follows the continental slope roughly along the 800 m isobath, except for between sections E and C (Figure 7). West of section C (at 18°E and 81.25°N) the objective interpolation shows a divergent field along the path of the boundary current. The divergence suggests a deviation from the average geostrophic flow and indicates a location with highly variable currents. We hypothesize that the shelf break near 18°E can be important for ejecting and distributing AW into the Sofia Deep. Along the southern rim of the Sofia Deep, the currents flow westward, consistent with the reverse flow observed at the seaward edge of our sections (Figure 4).

4.6. Wind forcing

The wind forcing was highly variable in the region north of Svalbard. Figure 8 shows the wind stress vector (τ) and wind stress curl ($\nabla \times \tau$), both as a time series from June to November (Figures 8a and 8b), and average conditions during the cruise periods and the different Seaglider sections (Figures 8c–8g). From Figures 8d (Fall cruise) to 8e (Seaglider section C_{Sg}) we see a large change in τ and $\nabla \times \tau$. During the cruise transect along section C (end of the Fall cruise), $\nabla \times \tau$ was negative over the Sofia Deep and the continental slope, and rapidly changed sign to positive at the time of the Seaglider transect. The dashed vertical line in Figure 8a separates the Fall cruise from the Seaglider transect. This rapid change in wind stress curl occurs at the same time as the volume transport through section C increases from 1.9 to 3.5 Sv, and is likely a geostrophic response to the change in sea surface height (η) forced by the wind, discussed in section 5.2.

The root-mean-squared (RMS) wind stress curl from the time series in Figure 8a was 0.43×10^{-6} N m^{-3}. Between 1 June and 30 November, we observed seven events with positive wind stress curl and six events with negative wind stress curl with magnitudes above one RMS value. The events lasted between 1 and 5 days, with the longest event being the positive anomaly during the Seaglider transect C_{Sg}.

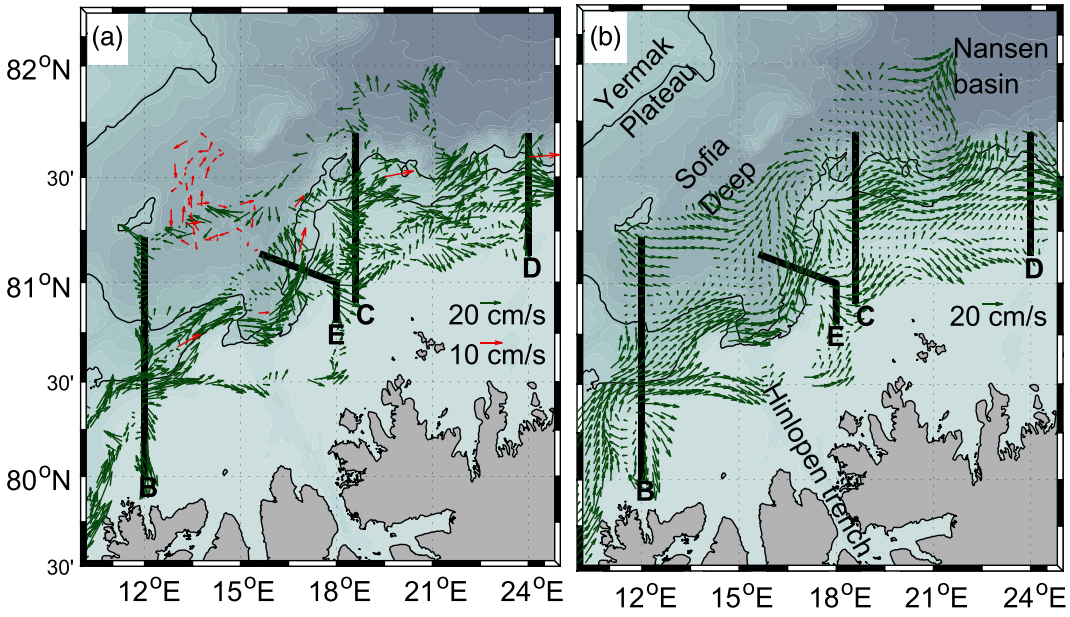

Figure 7. (a) Green arrows show 0–1,000 m depth-averaged currents, bin-averaged over 3 km by 3 km horizontal bins, from SADCPs, LADCPs, and Seaglider. Red arrows show drift trajectories from Argo floats. Note the different scale for the green and red arrows. (b) Objective interpolation of average currents in (a). Thick black lines show predefined sections. Black contours show the 800 and 1,500 m isobath.

4.7. Historical Data

Recent changes reported in the general hydrography and sea ice conditions of the Arctic Ocean motivate a comparison of our observations to the last decades. In Figure 9 we compare our summer through fall average hydrography (Figure 9a) to average hydrography from the last decade (Figure 9b) and pre-2008 data (Figure 9c), including relative u_g calculated from the obtained Θ and S_A sections. Historical data from June to November were binned in 5 km horizontal bins before interpolating and finally smoothed using a 20 m by 20 km (vertical by horizontal) moving average. Lacking velocity observations, we choose a common cross-slope width of AW between −40 and 40 km (between the 2,060 m and 110 m isobaths respectively on our average bathymetry) to compare the average AW properties (Table 3). Heat content is calculated as described in section 3.5, and salt content is calculated (instead of an ambiguous fresh water content) following Schauer and Losch (2019).

Heat and salt content in our summer-fall 2018 observations are between the values inferred for the past decade and pre-2008. The average AW layer during the past decade stands out as particularly warm and salty. However, we note that average Θ in the AW layer is nearly the same in our observations as the past decade and that the difference in heat content is due to a thicker AW layer during the past decade. The average S_A in the AW layer is the same in our observations as pre-2008. The two-core structure observed in our data has a stronger resemblance in the past decade than pre-2008, potentially related to a shrinking sea ice cover and stronger atmospheric forcing.

5. Discussion

5.1. Average Transport and Seasonality

We observed an average AW volume transport of 2.6 $\pm$0.2 Sv from our measurements from summer to late fall and between 12°E and 24°E north of Svalbard. From a cruise in September 2013, Pérez-Hernández et al. (2017) observed an AW volume transport of 2.3 $\pm$0.3 Sv farther east, between 21°E and 33°E. The transport estimated from a mooring array at 30°E during 2013, averaged over the open water season to be comparable to our measurements, was 2.4 $\pm$0.1 Sv (Pérez-Hernández et al., 2019). We note that the

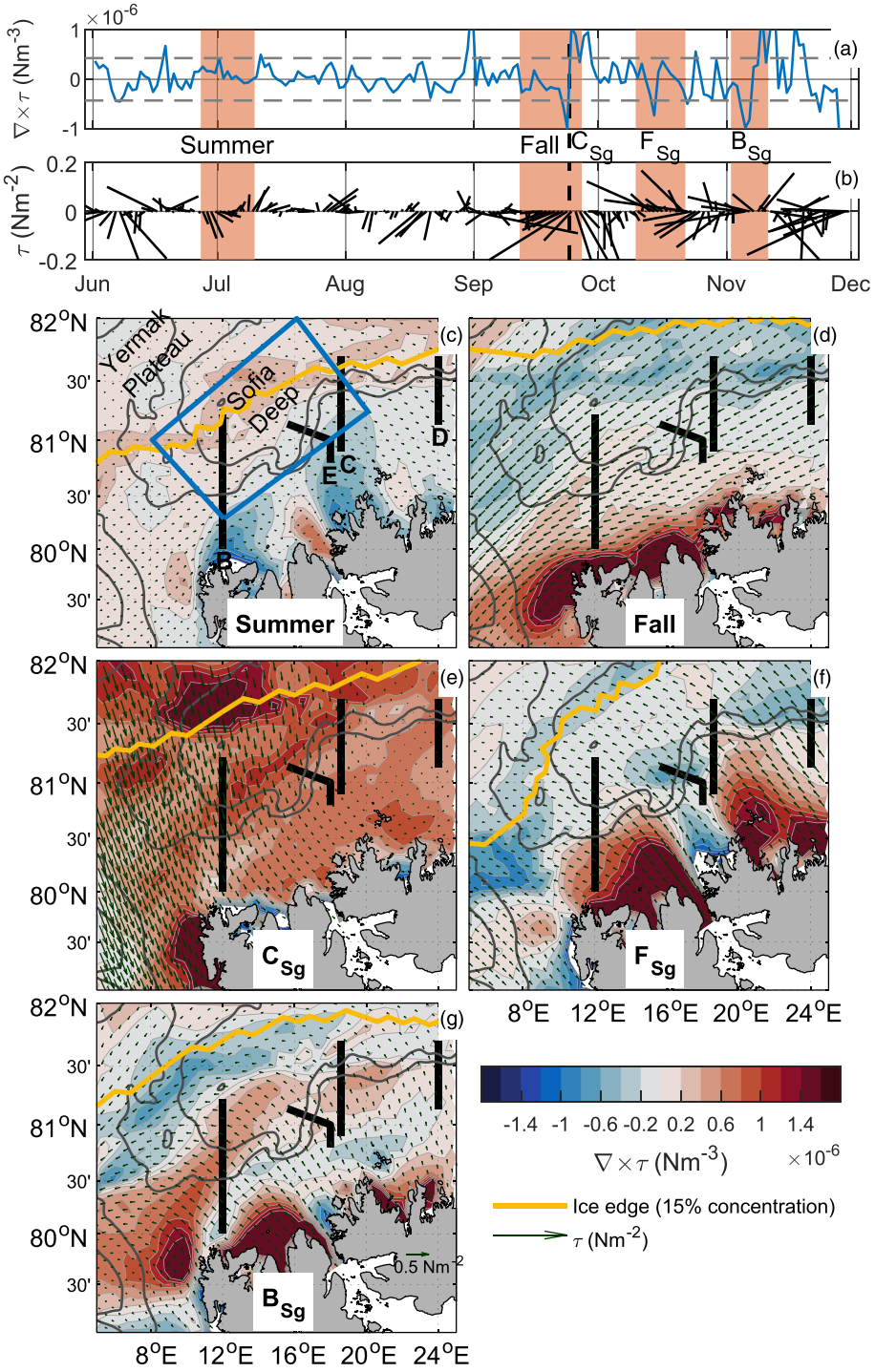

Figure 8. (a) Daily mean wind stress curl ($\nabla \times \tau$) averaged over the blue box shown in (c). Highlighted time periods indicate the times of the cruises and the Seaglider transects. Dashed black line separates the fall cruise from Seaglider transect C_{Sg}. Dashed gray lines indicate the root-mean-squared value. (b) Daily mean wind stress (τ) and wind stress direction averaged over the box in (c). c–g) Mean atmospheric conditions during the different cruises and Seaglider transects. Solid black lines indicate the predefined sections. Solid gray lines are the 800 and 1,500 m isobaths.

definition of AW used by Pérez-Hernández et al. (2017, 2019) differs from ours in the temperature criterion: They use $\Theta > 1$, whereas we use $\Theta > 2$. Our average AW volume transport estimate increases to 3.0 $\pm$0.2 Sv when the same definition as Pérez-Hernández et al. (2017, 2019) is used, that is, larger by 0.7 Sv than in

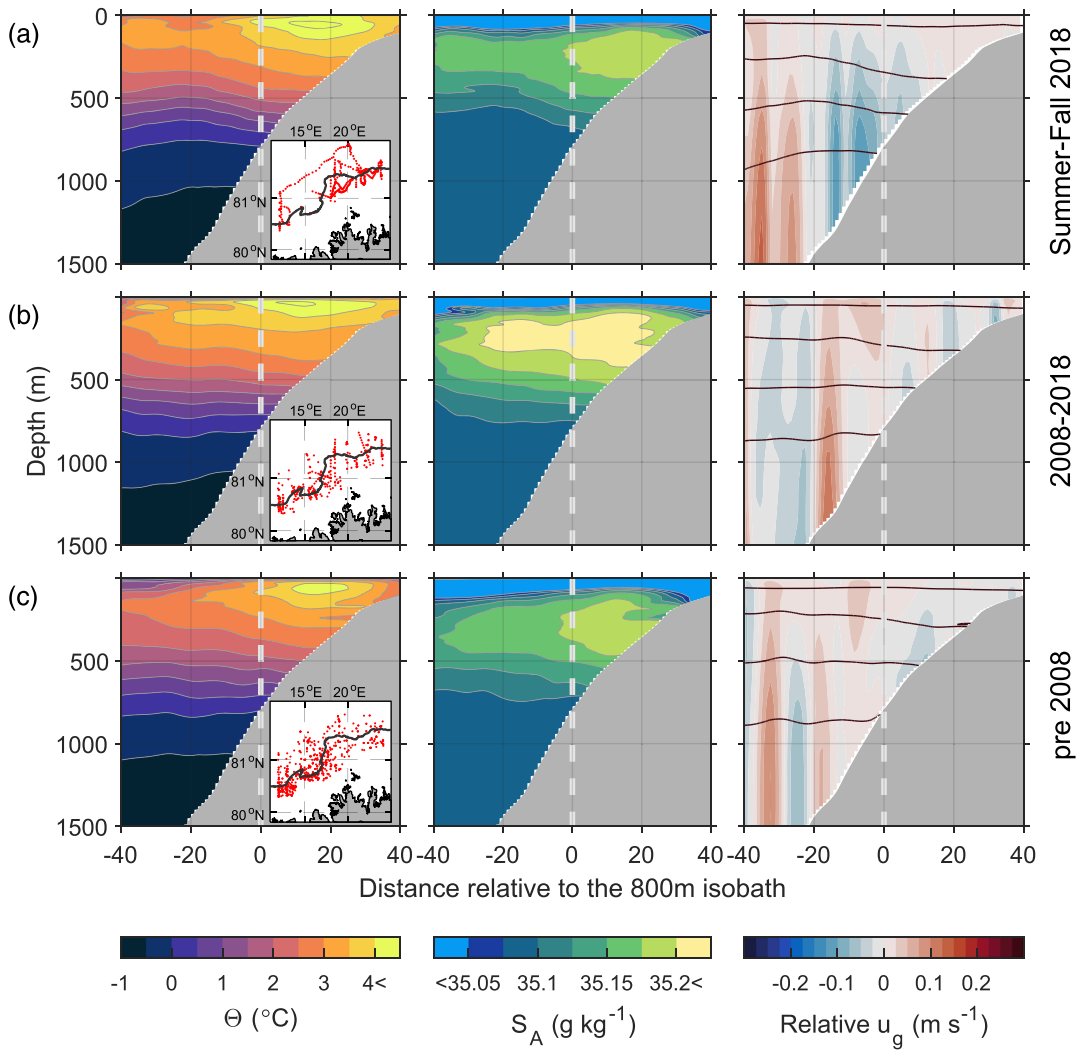

Figure 9. (a) Average composite sections, same as Figure 5a, but with relative u_g. (b) Average Θ, S_A, and relative u_g during June-November for the last 10 years (2008–2018). (c) Average Θ, S_A, and relative u_g during June-November for pre-2008. Black lines are isopycnals. The maps in the Θ plots show the CTD stations used for compiling the respective plots. The historical CTD data were fitted onto our average bathymetry similar to our composite sections.

Pérez-Hernández et al. (2019). However, the average volume transports reported by Pérez-Hernández et al. (2017, 2019) are observed further east than our sampling region, and we expect AW to gradually cool downstream. In addition, the mooring array at 30°E is located east of the Kvitøya Trough, where AW is known to enter and mix with colder shelf waters (Pérez-Hernández et al., 2017). Hence, our original temperature threshold estimate may be directly compared, which then agrees with the 2013 estimates to within errorbars. Nonetheless, this agreement can be fortuitous as we note that Våge et al. (2016) and Kolås and Fer (2018) reported smaller AW volume transports (1.6 ± 0.3 Sv and 1.3 Sv, respectively), which emphasizes the large volume transport variability observed north of Svalbard.

The boundary current north of Svalbard has a strong seasonal signal. We observed a 1 ± 0.3 Sv increase in the AW inflow from summer to fall, with a maximum of 3 Sv in October. This is comparable to the seasonality observed by the mooring array at 30°E (Pérez-Hernández et al., 2019). In the same period, we observed an increase in the velocity-weighted average AW temperature by 0.4 ± 0.2°C, which is less than the

Table 3
Calculations of Laterally and Vertically Integrated Heat and Salt Content Within AW Between −40 and 40 km

	Summer-fall 2018	2008–2018	Pre-2008
AW area (km^2)	27	29	24
$\overline{\Theta}$ (°C)	3.19	3.21	2.85
$\overline{S_A}$ (g kg^{-1})	35.15	35.17	35.15
Heat content (10^{14} J m^{-1})	3.5	3.8	2.8
Salt content (10^8 kg m^{-1})	9.6	10.5	8.5

Note. Calculations are based on the hydrography presented in Figure 9.

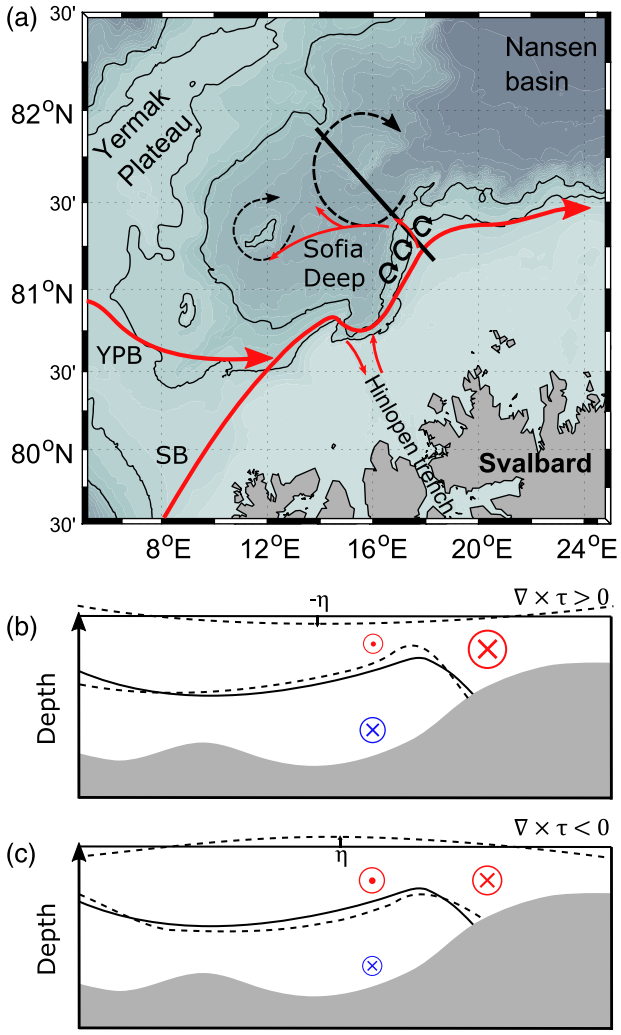

Figure 10. (a) Red arrows show the AW circulation in the study region. Black dashed arrows show possible anticyclonic circulation in the Sofia Deep. Small black arrows mark the possible generation site for eddies. The black line is the transect sketched in (b) and (c). Response of the circulation strength, sea level, and interface between the Atlantic Water and deeper water masses, to (b) a positive and (c) a negative wind stress curl in the Sofia Deep. For (b) and (c), solid line is the normal state, dashed line is perturbation from the wind stress curl.

0.84°C seasonal change observed by Pérez-Hernández et al. (2019). The seasonality of the AW inflow north of Svalbard is highly correlated with the volume transport of the WSC (Lique & Steele, 2012) and should be distinguished from the short-term and spatial variability north of Svalbard.

5.2. Spatial and Short-Term Variability

We observe large spatial and short-term variability in our synoptic sections north of Svalbard. Most noteworthy are the changes in volume transport of AW from section C (1.9 Sv) to D (1.4 Sv) and between C (1.9 Sv) and C_{Sg} (3.5 Sv). The change from C to D is likely partially explained by modification of AW due to heat loss to colder surrounding water and partially by the lack of observations on the shelf (Figure 3d). The change between sections C and C_{Sg}, only 5 days apart, tells a different story. There is a flow reversal on the shallow side of the first transect (Figure 3c); however, the reversal transport is only 0.1 Sv and does not explain why u_g in the entire AW layer is intensified during the second transect (Figure 3f). We suggest this increase in transport is related to the wind stress curl (section 4.6).

During the few days between conducting sections C and C_{Sg}, the average $\nabla \times \tau$ over the Sofia Deep changed from strongly negative (-10^6 N m^{-3}) to strongly positive (10^6 N m^{-3}) (Figure 8a). A schematic of expected response to anomalous wind stress curl events in the Sofia Deep is shown in Figures 10b and 10c. A negative $\nabla \times \tau$ event in the Sofia Deep would increase the sea surface height, η, in the Sofia Deep and decrease it on the continental shelf, thus act to weaken the AW boundary current. This is the effect we observed along section C during the Fall cruise (Figure 8d), where the boundary current weakened enough to cause a reversal on the shelf (Figure 3c). A positive $\nabla \times \tau$ event would have the opposite effect, decreasing η in the Sofia Deep and increasing η on the shelf, intensifying the boundary current and increasing the transport. This is the effect we observed a few days later during the Seaglider transect C_{Sg} (Figure 3f), following the abrupt change in wind stress curl (Figure 8e). Studies in the Chukchi Sea and Beaufort Sea show that η lags the onset of τ by about a day and that the geostrophic response to η, the balance between the pressure gradient force and Coriolis follows the change in η without any lag (Li et al., 2019; Lin et al., 2019). The geostrophic response to a change in η can be $\mathcal{O}(10)$ cm s^{-1} and can be strong enough to cause a reversal in the average flow (Lin et al., 2019). A similar mechanism has also been observed on the West Spitsbergen Shelf where winter cyclones are known to accelerate and widen the West Spitsbergen Current (Nilsen et al., 2016).

5.3. Bottom-Intensified Current and the AW Recirculation

The complex bathymetry in the region affects the circulation patterns. In addition to the AW boundary current, approximately centered at the 800 m isobath, we observe two features not previously discussed in literature, yet supported by previous observations. One is the westward flowing AW along the southern rim of the Sofia Deep (Figure 7), hereby referred to as the AW recirculation. The other feature is the bottom-intensified current following the continental slope roughly between the 1,500 and 1,800 m isobaths.

The bottom-intensified current on the lower continental slope is observed along sections B, C, and E (Figures 3a–3c). The slope of isopycnals in the deeper part of the Seaglider sections suggests the presence of a bottom-intensified current (Figures 3e–3g); however, the glider does not extend deep enough to resolve the current. This outer bottom-intensified current is seen in all composite sections, as well as the seasonal average (Figure 5) and is distinct in the volumetric $\Theta - S_A$ diagram (Figure 6). The bottom-intensified current mainly consists of Arctic Intermediate Water, and to a lesser extent cold Norwegian Sea Deep Water and

Eurasian Basin Deep Water (Figure 6). These water masses are common in the Eurasian Basin. Our water mass definitions are based on earlier work and recent changes in the Arctic Ocean could potentially affect the water mass limits.

Revisiting earlier published observations from this region, we note that bottom-intensified currents were occasionally measured north of Svalbard. In one of their transects, Våge et al. (2016) observed a bottom-intensified current along 30°E but did not further discuss it. Pérez-Hernández et al. (2017) discussed a bottom intensification of the AW layer as the AW meandered seawards but did not show any bottom intensification in the deeper parts. Our analysis of historical hydrographic observations from north of Svalbard suggests that the bottom-intensified flow near 1,500 m depth is a robust feature (Figure 9), both during the last decade and pre-2008, although its location on the slope may vary.

The bottom-intensified current and the AW boundary current are separated by shoaling deep isopycnals; see the black density lines in the composite sections (Figures 4 and 5). The positive isopycnal slope seaward of the bottom-intensified current is due to colder and saltier water found further up in the water column near the continental shelf than further out in the basin. This must be caused by either lifting the colder water up slope or depressing the water in the basin. Subinertial vorticity waves (e.g., coastal or topographically trapped waves), low frequency internal waves, or wind-induced upwelling could move deep, cold waters upslope; however, because the observations are robust in all composites (as well as in the multiyear averaged historical data), a local, transient lifting mechanism seems unlikely. Instead, we suggest the deeper isopycnals are being depressed in the Sofia Deep by an average anticyclonic circulation. The southern edge of this is captured by the negative geostrophic velocity near the deep end of our sections (Figure 3) and by the westward currents along the Seaglider track in the Sofia Deep (Figure 7). Cokelet et al. (2008) show an anticyclonic circulation in their section 3, crossing the Sofia Deep. They discuss the outer edges of their section as two separate domains and do not consider an anticyclonic circulation pattern. We propose these edges are likely linked and potentially related dynamically to the seamounts in the Sofia Deep. The isopycnals along section 3 of Cokelet et al. (2008) spread in the middle, supporting such an anticyclonic circulation.

However, our observations differ somewhat from those by Cokelet et al. (2008). They observed mostly barotropic currents, whereas we observe a baroclinic flow with the upper AW layer flowing westward and the deeper water flowing eastward. One reason for this difference may be that our higher resolution observations capture stronger cross-slope density gradients. The cross-slope density gradient may also be affected by the wind stress curl, thus periodically changing the strength of the bottom-intensified current.

The strength of the AW recirculation and the bottom-intensified flow is likely affected by the wind forcing, similar to the boundary current (section 5.2). Positive $\nabla \times \tau$ would decrease the barotropic counter current, while negative $\nabla \times \tau$ would increase it. In addition to the transient geostrophic set-up effect, a prolonged wind stress curl event in the Sofia Deep could cause upwelling or downwelling on the continental slope, affecting the isopycnal gradient and the strength of the bottom-intensified current (Figures 10b and 10c). Finally, upwelling will act to pull up the isopycnals separating the AW boundary current and the opposing flow, potentially creating a density barrier between the two. When the density barrier is strong, that is, prolonged positive $\nabla \times \tau$, we expect less interaction between the AW boundary current and the counter flow, whereas when the density barrier is weakened, that is, prolonged negative $\nabla \times \tau$, we expect more AW water to spread laterally.

Along our Seaglider track in the Sofia Deep, we do not observe one continuous AW layer but instead patches of AW with variable layer thickness and spreading isopycnals, suggesting several anticyclonic eddies (not shown). Thus it is likely that AW is not continuously fed into the anticyclonic circulation in the Sofia Deep but instead released from the AW boundary current as eddies.

Our interpretation finds support from numerical models and other observations. An eddy-resolving model (FESOM_1km) was used by Wekerle et al. (2017) to simulate the layer-averaged AW velocity for the region west and north of Svalbard in the period 2001–2009. Their results show a westward flowing current north of the eastward flowing boundary current (extending as far as 31°E) and an anticyclonic circulation in the Sofia Deep, supporting our observations. We also note that an average hydrographic section (constructed from eight cross-slope transects) near 31°E north of Svalbard shows an outer westward-flowing branch containing AW with a local salinity maximum (Pérez-Hernández et al., 2017).

An alternative hypothesis could be that our observations capture the southern edge of a standing eddy (not resolved with our data), possibly being fed by the anticyclones shed from the instability of the boundary current. It is common that the steepening slope, such as in our region, allow generation of eddies through baroclinic, barotropic or mixed instabilities (Dugstad et al., 2019; Isachsen, 2015). An example of such an eddy is the permanent Lofoten Basin eddy observed in the Norwegian Sea (see Bosse et al., 2019, and the references therein).

5.4. Method Sensitivity

In most of our observations, spatial variability and day-to-day variability cannot be distinguished. To complete a section, ship uses about a day, whereas the Seaglider uses several days. The variability captured along such a section is a combination of spatial and temporal variability. Several transects along the same section are needed to resolve such variability.

As we lacked repeated sections for most of our transects, a comparison between different cruises and different data sets is difficult. For that reason we decided to compile composite sections (as described in Section 3.3) even though the topography in the region is complex. However, moving the original data location along isobaths onto a section normal to the 800 m isobath can potentially change the horizontal temperature and salinity gradients, thus influencing the geostrophic velocity calculations. For example, if we calculate the average AW volume transport from a composite section consisting of only CTD stations along sections C and D, we obtain 2.4 $\pm$0.2 Sv, although the volume transport through sections C and D is only 1.9 and 1.4 Sv, respectively (Table 1). In this case our average bathymetry is not representative of the average slope along sections C and D and produces unrealistically large cross-slope gradients. Our average bathymetry is an average over the entire continental slope between 12°E and 24°E north of Svalbard and is chosen in order to minimize the change in horizontal gradient when the CTD stations used for the composite represent the same region.

Although the sections were carefully chosen in order to minimize the change in horizontal gradient, we tested the sensitivity by using an alternative method for calculating the Seaglider section F_{Sg}, which has a substantial scatter of station locations (Figure 1). Instead of moving data along isobaths we interpolated the data at their original location onto 1 dbar level grids, before choosing a section across the isobaths, roughly in the middle of our data cluster. This method increased the volume transport across the section by about 10%. In addition, throughout our analysis we have interpolated our sections onto a 1 km horizontal grid. Decreasing the horizontal resolution from 1 to 5 km reduced the transport by about 15%. However, a 5 km horizontal resolution is coarser than the ship's station resolution through the center of the core and is a too low resolution for realistic core transport estimates.

6. Summary

We analyzed hydrographic and current observations from two scientific cruises, one Seaglider mission and two Argo floats, during summer and fall 2018, north of Svalbard (Figure 1). We presented the data as synoptic sections, composite sections, and depth-averaged currents in order to resolve short-term variability, intraseasonal variability, and general circulation.

We suggest the AW circulation pattern presented in Figure 10a. Our observations showed the AW boundary current into the Arctic, following the 800 m isobath. North of the AW boundary current we observed an AW recirculation in the Sofia Deep, a return flow containing a separate patch of AW, overlaying an eastward flowing bottom-intensified current (Figures 4 and 5).

The boundary current north of Svalbard between 12°E and 24°E is highly variable both in time and space. We observed an average AW transport of 2.6 $\pm$0.2 Sv into the Arctic (Table 1). From summer to fall, the average AW transport increased from 2.0 $\pm$0.1 Sv to 3.0 $\pm$0.2 Sv, with a maximum in October. The short-term variations were even larger, for example two transects along the same section, only 5 days apart, showed an increase in AW transport from 1.9 to 3.5 Sv. This increase was caused by an abrupt change in wind stress curl from negative to positive in the Sofia Deep, strengthening the AW boundary current.

Figures 10b and 10c summarize the likely response to anomalous wind stress curl events in the Sofia Deep. A negative $\nabla \times \tau$ event (Figure 10c) in the Sofia Deep weakens the AW boundary current through a geostrophic

set-up effect and could potentially overcome the boundary current and lead to a reversal on the shelf (section C during the Fall cruise, Figure 3c). A positive $\nabla \times \tau$ event (Figure 10b) would have the opposite effect, intensify the boundary current and increase its transport (as in the Seaglider transect C_{Sg}, Figure 3f).

Also the strength of the return flow and the bottom-intensified flow is likely affected by the wind forcing, similar to the boundary current. In addition to a transient geostrophic set-up effect, a prolonged wind stress curl event in the Sofia Deep could cause upwelling or downwelling on the continental slope, modulating the isopycnal gradient and the strength of the bottom-intensified current (Figures 10b and 10c).

Finally, we note that section C, near 18°E, is a likely generation site for eddies that detach from the boundary current and are transported into the Sofia Deep. Signatures of multiple eddies were found along the Seaglider transect crossing the Sofia Deep and will be the subject of future analyses. Our data suggest the presence of an average anticyclonic circulation in the Sofia Deep, likely around each of the seamounts. However, the mechanism maintaining such an anticyclonic circulation is unclear and merits further studies.

Appendix A: Average Bathymetry for Composite Sections

Following a method similar to Fratantoni and Pickart (2007), we construct a composite section. Using full resolution data from IBCAO v3, we extracted bottom topography data along 30 sections normal to the 800 m isobath north of Svalbard, between 11°E and 24°E. Coordinates were transformed into Cartesian (x,z) coordinates, and the bottom data along the sections were interpolated onto a 1 km horizontal resolution grid. Next we calculated the inverse slope $[(dz/dx)^{-1}]$ and removed all points where the inverse slope was above 0, or less than −0.35 (vertical m/horizontal km)$^{-1}$. The median depth and median inverse slope were calculated for 50 m vertical bins between 150 and 2,500 m depth. We use the median instead of the average in order to exclude some outliers. For each bin, the inverse slope was multiplied by dz in order to obtain the horizontal displacement, dx. Finally, dx was summed and referenced to the horizontal location of the 800 m isobath. In our sections, negative dx is toward deep water and positive toward shallow waters.

When generating the composite sections, the following stations were excluded. For the summer cruise, data from the three southern-most stations along sections B and C required tens of kilometers relocation to fit the average bottom and were excluded. The southern-most station along section D and the northernmost station along section B were removed for both cruises because the bottom slope changes sign.

Appendix B: Error Calculations

For each section we subtracted the gridded section field from our measurements, retaining the residuals. Pairwise semivariance (variance divided by two) between the residuals was plotted against horizontal distance between the pairs of the residuals, obtaining a so-called semivariogram. An example is shown in Figure B1. Next, we fitted a Gaussian variogram model to our empirical variogram using the following equation (ch. 2.4 Cressie, 1993):

$$\gamma(d) = (\sigma^2 - \nu)\left(1 - exp\left(-3\frac{d^2}{r^2}\right)\right) + \nu \quad \text{(B1)}$$

where σ^2 is the saturation value at which the variogram stabilises (the sill), r is the distance where the variogram reaches the sill, ν is the zero-crossing value of the variogram, and d is the distance between the pairs of residuals. Knowing the horizontal distance between any grid point in our gridded field and the closest measurement, we computed semivariance matrices. Instrumental errors were added to the variance before taking the square root, obtaining the one-sided standard deviation at any grid point. One thousand Gaussian distributed random error matrices, using the obtained standard deviation, were added to each section, including composite sections. Reported errors are the root-mean-square of the difference between calculations from the original gridded field and each of the fields including the random error

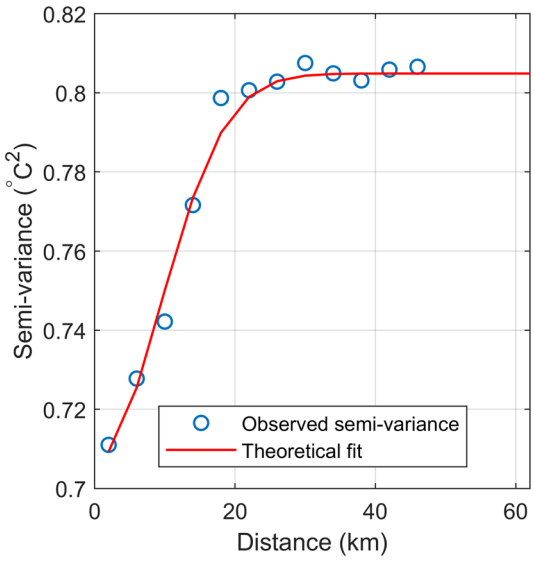

Figure B1. Variogram showing semivariance of Θ versus distance between residuals.

matrices. For Θ, S_A and volume transport, the errors are rounded up to the nearest 0.1°C, 0.01 g kg^{-1}, and 0.1 Sv, respectively.

Data Availability Statement

All data are available from the Norwegian Marine Data Centre; data sets from the July cruise (KB 2018616) are available at https://doi.org/10.21335/NMDC-2047975397, data sets from the September cruise (KH 2018709) are available at https://doi.org/10.21335/NMDC-2039932526, and the glider data are available online (https://doi.org/10.21335/NMDC-1841837601). The historical data are available from the University Centre in Svalbard (https://doi.org/10.21334/unis-hydrography). The ice edge data are available online (https://thredds.met.no/thredds/osisaf/osisaf_seaiceedge.html). Argo float data are available from https://argo.jcommops.org, using the identification numbers 6903548 and 3901910.

Acknowledgments

This work was supported by the Nansen Legacy Project, project number 276730. We thank the officers, crew and scientist of the *RV Kristine Bonnevie* cruise in July 2018 and of the *RV Kronprins Haakon*cruise in September 2018. We thank the glider team at NorGliders (http://norgliders.gfi.uib.no/). We thank two anonymous reviewers whose comments helped improve a previous version of this paper.

References

Aagaard, K., Foldvik, A., & Hillman, S. R. (1987). The West Spitsbergen Current: Disposition and water mass transformation. *Journal of Geophysical Research*, *92*(C4), 3778. https://doi.org/10.1029/jc092ic04p03778

Aagaard, K., Swift, J. H., & Carmack, E. C. (1985). Thermohaline circulation in the Arctic Mediterranean Seas. *Journal of Geophysical Research*, *90*(C3), 4833–4846. https://doi.org/10.1029/jc090ic03p04833

Böhme, L., & Send, U. (2005). Objective analyses of hydrographic data for referencing profiling float salinities in highly variable environments. *Deep Sea Research Part II: Topical Studies in Oceanography*, *52*(3-4), 651–664. https://doi.org/10.1016/j.dsr2.2004.12.014

Beszczynska-Möller, A., Fahrbach, E., Schauer, U., & Hansen, E. (2012). Variability in Atlantic water temperature and transport at the entrance to the Arctic Ocean, 1997–2010. *ICES Journal of Marine Science*, *69*(5), 852–863. https://doi.org/10.1093/icesjms/fss056

Bosse, A., Fer, I., Lilly, J. M., & Søiland, H. (2019). Dynamical controls on the longevity of a non-linear vortex: The case of the Lofoten Basin Eddy. *Scientific Reports*, *9*(1), 13448. https://doi.org/10.1038/s41598-019-49599-8

Bourke, R. H., Weigel, A. M., & Paquette, R. G. (1988). The westward turning branch of the West Spitsbergen Current. *Journal of Geophysical Research*, *93*(C11), 14065. https://doi.org/10.1029/jc093ic11p14065

Boyd, T. J., & D'Asaro, E. A. (1994). Cooling of the West Spitsbergen Current: Wintertime observations West of Svalbard. *Journal of Geophysical Research*, *99*(C11), 22,597–22,618. https://doi.org/10.1029/94jc01824

Carmack, E., Polyakov, I., Padman, L., Fer, I., Hunke, E., Hutchings, J., et al. (2015). Toward quantifying the increasing role of oceanic heat in sea ice loss in the New Arctic. *Bulletin of the American Meteorological Society*, *96*(12), 2079–2105. https://doi.org/10.1175/bams-d-13-00177.1

Cokelet, E. D., Tervalon, N., & Bellingham, J. G. (2008). Hydrography of the West Spitsbergen Current, Svalbard Branch: Autumn 2001. *Journal of Geophysical Research*, *113*, C01006. https://doi.org/10.1029/2007jc004150

Cressie, N. A. C. (1993). *Statistics for spatial data* (2nd ed.). New York: Wiley-Interscience Publication.

Crews, L., Sundfjord, A., Albretsen, J., & Hattermann, T. (2018). Mesoscale eddy activity and transport in the Atlantic water inflow region north of Svalbard. *Journal of Geophysical Research: Oceans*, *123*, 201–215. https://doi.org/10.1002/2017JC013198

Crews, L., Sundfjord, A., & Hattermann, T. (2019). How the Yermak Pass Branch regulates Atlantic water inflow to the Arctic Ocean. *Journal of Geophysical Research: Oceans*, *124*, 267–280. https://doi.org/10.1029/2018JC014476

Dugstad, J., Fer, I., LaCasce, J., de La Lama, M. S., & Trodahl, M. (2019). Lateral heat transport in the Lofoten Basin: Near-surface pathways and subsurface exchange. *Journal of Geophysical Research: Oceans*, *124*, 2992–3006. https://doi.org/10.1029/2018jc014774

Erofeeva, S., & Egbert, G. (2020). Arc5km2018: Arctic Ocean inverse tide model on a 5 kilometer grid, 2018. Arctic Data Center. https://doi.org/10.18739/A21R6N14K

Fer, I., Koenig, Z., Bosse, A., Falck, E., Kolås, E., & Nilsen, F. (2020). *Physical oceanography data from the cruise KB 2018616 with R.V. Kristine Bonnevie*. Bergen: University of Bergen. https://doi.org/10.21335/NMDC-2047975397

Fer, I., Koenig, Z., Kolås, E., Falck, E., Fossum, T., Ludvigsen, M., et al. (2019). *Physical oceanography data from the cruise KH 2018709 with R.V. Kronprins Haakon, 12–24 September 2018*. Bergen: University of Bergen. https://doi.org/10.21335/NMDC-2039932526

Fer, I., Skogseth, R., & Geyer, F. (2010). Internal waves and mixing in the marginal ice zone near the Yermak Plateau. *Journal of Physical Oceanography*, *40*(7), 1613–1630. https://doi.org/10.1175/2010jpo4371.1

Firing, E., & Ranada, J. (1995). Processing ADCP data with the CODAS software system version 3.1. [Computer software manual].

Frajka-Williams, E., Eriksen, C. C., Rhines, P. B., & Harcourt, R. R. (2011). Determining vertical water velocities from Seaglider. *Journal of Atmospheric and Oceanic Technology*, *28*(12), 1641–1656. https://doi.org/10.1175/2011jtecho830.1

Fratantoni, P. S., & Pickart, R. S. (2007). The Western North Atlantic shelfbreak current system in summer. *Journal of Physical Oceanography*, *37*(10), 2509–2533. https://doi.org/10.1175/jpo3123.1

Garau, B., Ruiz, S., Zhang, W. G., Pascual, A., Heslop, E., Kerfoot, J., & Tintoré, J. (2011). Thermal lag correction on Slocum CTD glider data. *Journal of Atmospheric and Oceanic Technology*, *28*(9), 1065–1071. https://doi.org/10.1175/jtech-d-10-05030.1

Gascard, J.-C., Richez, C., & Rouault, C. (2013). New insights on large-scale oceanography in Fram Strait: The West Spitsbergen current. In *Arctic oceanography: Marginal ice zones and continental shelves* (pp. 131–182). Washington, DC: American Geophysical Union. https://doi.org/10.1029/CE049p0131

Hattermann, T., Isachsen, P. E., von Appen, W.-J., Albretsen, J., & Sundfjord, A. (2016). Eddy-driven recirculation of Atlantic Water in Fram Strait. *Geophysical Research Letters*, *43*, 3406–3414. https://doi.org/10.1002/2016gl068323

IOC, SCOR, & IAPSO (2010). The international thermodynamic equation of seawater 2010: Calculations and use of thermodynamic properties (Intergovernmental Oceanographic Commission, Manuals and Guides No. 56 ed.) [Computer software manual]. UNESCO.

International Argo Program (2003). Temperature, salinity, pressure, and biogeochemical profile data from globally distributed Argo profiling floats, by month since April 2003 for the Global Argo Data Repository, containing data from 1995-09-07 to present. [WMO Id 6903548 and 3901910]. NOAA National Centers for Environmental Information. Dataset. (Accessed on 15.11.2019) https://doi.org/10.25921/q97e-d719

Isachsen, P. E. (2015). Baroclinic instability and the mesoscale eddy field around the Lofoten Basin. *Journal of Geophysical Research: Oceans*, *120*, 2884–2903. https://doi.org/10.1002/2014jc010448

Jakobsson, M., Mayer, L., Coakley, B., Dowdeswell, J. A., Forbes, S., Fridman, B., et al. (2012). The International Bathymetric Chart of the Arctic Ocean (IBCAO) Version 3.0. *Geophysical Research Letters*, *39*, L12609. https://doi.org/10.1029/2012gl052219

Koenig, Z., Provost, C., Sennéchael, N., Garric, G., & Gascard, J.-C. (2017). The Yermak Pass Branch: A major pathway for the Atlantic water north of Svalbard? *Journal of Geophysical Research: Oceans*, *122*, 9332–9349. https://doi.org/10.1002/2017jc013271

Kolås, E., & Fer, I. (2018). Hydrography, transport and mixing of the West Spitsbergen Current: The Svalbard Branch in summer 2015. *Ocean Science*, *14*(6), 1603–1618. https://doi.org/10.5194/os-14-1603-2018

Kolås, E., & Fer, I. (2020). *Physical oceanography data from a Seaglider mission north of Svalbard, late fall 2018*. Bergen: University of Bergen. https://doi.org/10.21335/NMDC-1841837601

Large, W. G., & Pond, S. (1981). Open ocean momentum flux measurements in moderate to strong winds. *Journal of Physical Oceanography*, *11*(3), 324–336.

Li, M., Pickart, R. S., Spall, M. A., Weingartner, T. J., Lin, P., Moore, G. W. K., & Qi, Y. (2019). Circulation of the Chukchi Sea shelfbreak and slope from moored timeseries. *Progress in Oceanography*, *172*, 14–33. https://doi.org/10.1016/j.pocean.2019.01.002

Lin, P., Pickart, R. S., Moore, G. W. K., Spall, M. A., & Hu, J. (2019). Characteristics and dynamics of wind-driven upwelling in the Alaskan Beaufort Sea based on six years of mooring data. *Deep Sea Research Part II: Topical Studies in Oceanography*, *162*, 79–92. https://doi.org/10.1016/j.dsr2.2018.01.002

Lique, C., & Steele, M. (2012). Where can we find a seasonal cycle of the Atlantic water temperature within the Arctic Basin? *Journal of Geophysical Research*, *117*, C03026. https://doi.org/10.1029/2011JC007612

Manley, T. O. (1995). Branching of Atlantic Water within the Greenland-Spitsbergen Passage: An estimate of recirculation. *Journal of Geophysical Research*, *100*(C10), 20627. https://doi.org/10.1029/95jc01251

Marnela, M., Rudels, B., Houssais, M.-N., Beszczynska-Möller, A., & Eriksson, P. B. (2013). Recirculation in the Fram Strait and transports of water in and north of the Fram Strait derived from CTD data. *Ocean Science*, *9*(3), 499–519. https://doi.org/10.5194/os-9-499-2013

McDougall, T. J. (2003). Potential enthalpy: A conservative oceanic variable for evaluating heat content and heat fluxes. *Journal of Physical Oceanography*, *33*(5), 945–963. https://doi.org/10.1175/1520-0485(2003)033<0945:PEACOV>2.0.CO;2

McDougall, T. J., & Barker, P. M. (2011). Getting started with TEOS-10 and the Gibbs Seawater (GSW) oceanographic toolbox. SCOR/IAPSO WG127, 28 pp.

Menze, S., Ingvaldsen, R. B., Haugan, P., Fer, I., Sundfjord, A., Beszczynska-Möller, A., & Falk-Petersen, S. (2019). Atlantic water pathways along the north-western Svalbard shelf mapped using vessel-mounted current profilers. *Journal of Geophysical Research: Oceans*, *124*, 1699–1716. https://doi.org/10.1029/2018jc014299

Meyer, A., Fer, I., Sundfjord, A., & Peterson, A. K. (2017). Mixing rates and vertical heat fluxes north of Svalbard from Arctic winter to spring. *Journal of Geophysical Research: Oceans*, *122*, 4569–4586. https://doi.org/10.1002/2016jc012441

Meyer, A., Sundfjord, A., Fer, I., Provost, C., Robineau, N. V., Koenig, Z., et al. (2017). Winter to summer oceanographic observations in the Arctic Ocean north of Svalbard. *Journal of Geophysical Research: Oceans*, *122*, 6218–6237. https://doi.org/10.1002/2016jc012391

Nilsen, F., Skogseth, R., Vaardal-Lunde, J., & Inall, M. (2016). A simple shelf circulation model: Intrusion of Atlantic water on the west Spitsbergen shelf. *Journal of Physical Oceanography*, *46*(4), 1209–1230. https://doi.org/10.1175/jpo-d-15-0058.1

Onarheim, I. H., Smedsrud, L. H., Ingvaldsen, R. B., & Nilsen, F. (2014). Loss of sea ice during winter north of Svalbard. *Tellus A: Dynamic Meteorology and Oceanography*, *66*(1), 23,933–23,941. https://doi.org/10.3402/tellusa.v66.23933

Pérez-Hernández, M. D., Pickart, R. S., Pavlov, V., Våge, K., Ingvaldsen, R., Sundfjord, A., et al. (2017). The Atlantic water boundary current north of Svalbard in late summer. *Journal of Geophysical Research: Oceans*, *122*, 2269–2290. https://doi.org/10.1002/2016jc012486

Pérez-Hernández, M. D., Pickart, R. S., Torres, D. J., Bahr, F., Sundfjord, A., Ingvaldsen, R., et al. (2019). Structure, transport and seasonality of the Atlantic water boundary current north of Svalbard: Results from a year-long mooring array. *Journal of Geophysical Research: Oceans*, *124*, 1679–1698. https://doi.org/10.1029/2018jc014759

Perkin, R. G., & Lewis, E. L. (1984). Mixing in the west Spitsbergen current. *Journal of Physical Oceanography*, *14*(8), 1315–1325. https://doi.org/10.1175/1520-0485(1984)014<1315:MITWSC>2.0.CO;2

Pickart, R. S., & Smethie, W. M. (1998). Temporal evolution of the deep western boundary current where it enters the sub-tropical domain. *Deep Sea Research Part I: Oceanographic Research Papers*, *45*(7), 1053–1083. https://doi.org/10.1016/s0967-0637(97)00084-8

Polyakov, I. V., Pnyushkov, A. V., Alkire, M. B., Ashik, I. M., Baumann, T. M., Carmack, E. C., et al. (2017). Greater role for Atlantic inflows on sea-ice loss in the Eurasian Basin of the Arctic Ocean. *Science*, *356*(6335), 285–291. https://doi.org/10.1126/science.aai8204

Reistad, M., Breivik, O., Haakenstad, H., Aarnes, O. J., Furevik, B. R., & Bidlot, J.-R. (2011). A high-resolution hindcast of wind and waves for the North Sea, the Norwegian Sea, and the Barents Sea. *Journal of Geophysical Research*, *116*, C05019. https://doi.org/10.1029/2010jc006402

Rudels, B., Björk, G., Nilsson, J., Winsor, P., Lake, I., & Nohr, C. (2005). The interaction between waters from the Arctic Ocean and the Nordic Seas north of Fram Strait and along the East Greenland Current: Results from the Arctic Ocean-02 Oden expedition. *Journal of Marine Systems*, *55*(1-2), 1–30. https://doi.org/10.1016/j.jmarsys.2004.06.008

Rudels, B., Muench, R. D., Gunn, J., Schauer, U., & Friedrich, H. J. (2000). Evolution of the Arctic Ocean boundary current north of the Siberian shelves. *Journal of Marine Systems*, *25*(1), 77–99. https://doi.org/10.1016/s0924-7963(00)00009-9

Saloranta, T. M., & Haugan, P. M. (2004). Northward cooling and freshening of the warm core of the west Spitsbergen current. *Polar Research*, *23*(1), 79–88. https://doi.org/10.3402/polar.v23i1.6268

Schauer, U., & Losch, M. (2019). Freshwater in the ocean is not a useful parameter in climate research. *Journal of Physical Oceanography*, *2019*, 2309–2321. https://doi.org/10.1175/JPO-D-19-0102.1

Schlichtholz, P., & Houssais, M.-N. (2002). An overview of the θ - S correlations in Fram Strait based on the MIZEX 84 data. *Oceanologia*, *44*(2), 243–272.

Seaglider Quality Control Manual (2012). (Version 1.11 ed.) [Computer software manual].

Sirevaag, A., & Fer, I. (2009). Early spring oceanic heat fluxes and mixing observed from drift stations north of Svalbard. *Journal of Physical Oceanography*, *39*(12), 3049–3069. https://doi.org/10.1175/2009jpo4172.1

Skogseth, R., Ellingsen, P., Berge, J., Cottier, F., Falk-Petersen, S., Ivanov, B., et al. (2019). *UNIS hydrographic database*. Tromsø: Norwegian Polar Institute. https://doi.org/10.21334/unis-hydrography

Smith, W. H. F., & Wessel, P. (1990). Gridding with continuous curvature splines in tension. *Geophysics*, *55*(3), 293–305. https://doi.org/10.1190/1.1442837

Swift, J. H., & Aagaard, K. (1981). Seasonal transitions and water mass formation in the Iceland and Greenland seas. *Deep Sea Research Part A. Oceanographic Research Papers*, *28*(10), 1107–1129. https://doi.org/10.1016/0198-0149(81)90050-9

Uppala, S. M., Kållberg, P. W., Simmons, A. J., Andreae, U., Da Costa Bechtold, V., Fiorino, M., et al. (2005). The ERA-40 re-analysis. *Quarterly Journal of the Royal Meteorological Society: A journal of the atmospheric sciences, applied meteorology and physical oceanography*, *131*(612), 2961–3012.

Våge, K., Pickart, R. S., Pavlov, V., Lin, P., Torres, D. J., Ingvaldsen, R., et al. (2016). The Atlantic water boundary current in the Nansen Basin: Transport and mechanisms of lateral exchange. *Journal of Geophysical Research: Oceans*, *121*, 6946–6960. https://doi.org/10.1002/2016jc011715

Visbeck, M. (2002). Deep velocity profiling using lowered acoustic Doppler current profilers: Bottom track and inverse solutions. *Journal of Atmospheric and Oceanic Technology*, *19*(5), 794–807. https://doi.org/10.1175/1520-0426(2002)019<0794:DVPULA>2.0.CO;2

von Appen, W.-J., Schauer, U., Hattermann, T., & Beszczynska-Möller, A. (2016). Seasonal cycle of mesoscale instability of the west Spitsbergen current. *Journal of Physical Oceanography*, *46*(4), 1231–1254. https://doi.org/10.1175/jpo-d-15-0184.1

Wekerle, C., Wang, Q., von Appen, W.-J., Danilov, S., Schourup-Kristensen, V., & Jung, T. (2017). Eddy-resolving simulation of the Atlantic water circulation in the Fram Strait with focus on the seasonal cycle. *Journal of Geophysical Research: Oceans*, *122*, 8385–8405. https://doi.org/10.1002/2017jc012974